**Taisiya G. Kopytova**
Max-Planck-Institut für Astronomie

**Heidelberg 2016**

*Dissertation in Astronomy*
**submitted to the**
**Combined Faculties of the Natural Sciences and Mathematics**
**of the Ruperto-Carola-University of Heidelberg, Germany,**
**for the degree of**
***Doctor of Natural Sciences***

**Put forward by**
**M.Sc. *Taisiya G. Kopytova***
**born in Krasnoturinsk, Russia**

**Oral examination: 23.09.16**

# Characterization of stellar and sub-stellar atmospheres

**Taisiya G. Kopytova**
Max-Planck-Institut für Astronomie

**Referees:** **Prof. Dr. Thomas Henning**
**Prof. Dr. Ralf S. Klessen**

*To my mom*

# Zusammenfassung

In dieser Arbeit ziele ich auf die Charakterisierung einer Anzahl von (sub-) stellaren Begleitern ab. Bei der Untersuchung isolierter braune Zwerge, sehr massearmer Sterne und direkt beobachteter Exoplaneten mit insignifikanten Bahnbewegungen müssen wir uns auf theoretische Modelle verlassen um grundlegende Eigenschaften wie Masse, Alter und daraus folgend Effektivtemperatur und Schwerebeschleunigung an der Oberfläche abzuleiten. Gerade weil Stern- und Atmosphärenmodelle rasch weiterentwickelt werden, brauchen wir ein schlagkräftiges Handwerkszeug um sie zu testen und zu eichen.

Der Vergleich von aus Sternaufbau- und Atmosphärenmodellen berechneten Isochronen mit der beobachteten Sequenz in offenen Sternhaufen bietet eine Möglichkeit zur Überprüfung der Modelle. In offenen Sternhaufen befinden sich viele gleich alte Objekte der gleichen chemischen Zusammensetzung, die sich nur durch ihre Masse unterscheiden. Ich verwende unsere "Lucky Imaging"-Beobachtungen und Literaturdaten zur Ableitung der Einzelsternsequenz des offenen Sternhaufens der Hyaden. Ich vergleiche diese beobachtete Einzelsternsequenz mit theoretischen Isochronen um systematische Abweichungen und mögliche Probleme in den Modellen herauszustellen.

Allerdings gibt es viele Fälle in denen ein Test der Modelle vor ihrer Anwendung nicht m?glich ist. Ein Bespiel ist die Anwendung von Atmosphärenmodellen zur Bestimmung der Eigenschaften von WISE 0855-07, dem kühlsten der bisher bekannten Y-Zwerge. Ich zeige die durch unverstandene systematische Fehler in den Modellen und Beobachtungen gesteckten Grenzen bei der Bestimmung der Effektivtemperatur und bei Schlussfolgerungen über das Vorhandensein oder die Abwesenheit von Wasserdampfwolken auf.

Im dritten Abschnitt führe ich eine neue Methode zur Berücksichtigung der oben erwähnten systematischen Abweichungen ein. Hierzu leite ich einen "systematischen Vektor" ab, welcher eine Bestimmung der problematischen Wellenlängenbereiche bei der Anpassungen der Modellatmosphären an die beobachteten Infrarotspektren brauner Zwerge und direkt abgebildeter Exoplaneten ermöglicht. Diese Vorgehensweise ist von grundlegender Bedeutung bei der Bestimmung von Elementhäufigkeiten, inbesonder des C/O-Verhältnisses. Dieses Verhältnis ist ein wichtiger Parameter in Entstehungsszenarien von braunen Zwergen und Exoplaneten. Ich demonstriere eine Methode zur Bestimmung dieses Verhältnisses unter Vermeidung und Ausschließung der systematischen Effekte. Dies f?hrt zu einer signifikanten Verbesserung bei der Bestimmung des C/O-Verhältnisses, und erlaubt mir zuverlässigere Rückschlüsse auf die Einstehungsgeschichte ausgewählter Exoplaneten und braunen Zwerge.

# Abstract

In this work I aim characterize a number of (sub)-stellar companions. When studying isolated brown dwarfs, very low-mass stars, and directly imaged exoplanets with insignificant orbital motion, we have to rely on theoretical models to determine basic parameters such as mass, age, and consequently, effective temperature and surface gravity. While stellar and atmospheric models are rapidly evolving, we need a powerful tool to test and calibrate them.

One way to test models is to compare theoretical isochrones produced by interior and atmospheric models with observed sequences in open clusters. Open clusters contain many objects of the same chemical composition and age, and spanning a range of masses. Using our own Lucky imaging observations and literature data, I constructed a single-star sequence for the Hyades open cluster. I compare the obtained sequence to a set of theoretical isochrones identifying systematic offsets and revealing probable issues in the models.

However, there are many cases when it is impossible to test models before applying them to observations. One example is applying atmospheric models for constraining parameters of the coolest known Y dwarf WISE 0855-07. I demonstrate the limits of constraining effective temperature and the presence/absence of water clouds that are introduced by unknown systematic effects in models and observations.

In the final chapter I introduce a novel method to take into account the above-mentioned systematics. I construct a ”systematics vector” that allows us to reveal problematic wavelength ranges when fitting atmospheric models to observed near-infrared spectra of brown dwarfs and directly imaged exoplanets. This approach plays a crucial role when retrieving abundances of brown dwarfs and exoplanets, in particularly, a C/O ratio. The latter parameter is an important key to formation scenarios of brown dwarf and exoplanets. I show the way of constraining this parameter while eliminating systematics effects, which significantly improves the reliability of a final result and our conclusions about formation history of certain exoplanets and brown dwarfs.

# Contents

# Chapter 1

# Introduction

> *"The Uncertainty Principle. It proves we can't ever really know... what's going on. So it shouldn't bother you. Not being able to figure anything out. Although you will be responsible for this on the mid-term."*
>
> — A Serious Man, Dir. Ethan and Joel Coen, 2009

Observations of stars, brown dwarfs, and exoplanets provide understanding of their physics and, in some examples, give a key to their formation and evolution. By comparing observed quantities with the ones obtained from theoretical models we can test and improve our current knowledge of stellar and sub-stellar objects and, in case of well-trusted theoretical predictions, determine physical parameters for these objects by applying the models.

First of all, a nomenclature must be clarified. "A star is a self-gravitating celestial object in which there is, or there once was, sustained thermonuclear fusion of hydrogen in their core" (LeBlanc 2010). The main feature distinguishing brown dwarfs from stars is that, due to their lower mass ($\leq$ 0.08 $M_\odot$), they will never be able to collapse to the point where they have high enough density and, consequentially, high enough temperature in their interiors ($\sim 10^7$ K) to sustain thermonuclear fusion of hydrogen-1 in the core. On the other hand, brown dwarfs are able to fuse hydrogen-2 (deuterium), since the temperature needed for this thermonuclear reaction is lower ($\sim 10^7$ K). However, the internal energy produced by deuterium fusion is not enough to resist gravitational collapse, and brown dwarfs contract and cool down with age. The cooling down during contraction is due the electron degeneracy that is present in interiors of brown dwarfs. The existence of brown dwarfs was theoretically predicted by Kumar (1963) and Hayashi & Nakano

(1963) and the first brown dwarfs were discovered by Nakajima et al. (1995), Oppenheimer et al. (1995), and Rebolo et al. (1995). In contrast to brown dwarfs, planets are not expected to sustain deuterium fusion in their interiors ("deuterium burning limit", theoretically predicted at 13 $M_{Jup}$, e.g., Burrows et al. 1997) and should orbit a star. However, this definition has become less strict, because on the one hand, a number of free-floating objects with a mass $< 13$ $M_{Jup}$ have been discovered, and on the other hand, some of the planetary-like systems consist of companions with masses higher than the deuterium burning limit.

Stars, brown dwarfs, and exoplanets have distinguishably different interior and atmospheres that are key to their physical properties (effective temperature, surface gravity, chemical composition. These properties are usually retrieved by comparing observing data to theoretical predictions calculated for sets of different parameters. Different implementations of interior structure and atmospheric models exist, with different prescriptions of equations of state, nuclear energy production rates, atomic and molecular opacities, elemental abundances, etc. Therefore it is of prime importance to test and calibrate theoretical models by comparison with large and homogeneous observational data sets, and by pushing the observational sample towards lower masses and lower effective temperatures. That is why it is of high importance to have both well-analyzed data and reliable theoretical models to study and understand the atmospheres of stellar and sub-stellar objects. In this Chapter I will give a brief overview of (sub-)stellar interior and atmospheric models, as well as of some observational techniques. This overview is directly connected to my dissertation research, where I attempted to characterize a number of (sub-)stellar objects and to provide a benchmark for testing interior and atmospheric models.

## 1.1 Properties of brown dwarfs and directly imaged exoplanets

### 1.1.1 Spectral classification

After the discovery of brown dwarfs, it became clear that the classical "OBAFGKM" scheme for stellar spectral classification needs to be updated to include those new objects. The in $H$ (1.63 m$\mu$) and $K$ (2.2 m$\mu$) band observations of one of the first discovered brown dwarfs, Gl 229 B, showed clear $CH_4$ absorption (Oppenheimer et al. 1995), which strongly resembles the spectrum of Jupiter. Kirkpatrick (2005) published a review describing attempts to upgrade the spectral classification scheme, in order to include L and T classes for brown dwarfs. Recently, a number of Y dwarfs have been discovered (e.g., Cushing et al. 2011; Kirkpatrick et al. 2012, 2013; Liu et al. 2012; Tinney et al. 2012; Luhman 2014), which are the coolest sub-stellar objects and bridging the gap between hotter L and T dwarfs and giant exoplanets. For most of the spectral range, the brown dwarf "LTY" sequence is the temperature sequence. However, as reported by Filippazzo et al. (2015), low-gravity L dwarfs (younger than 100–200 Myr) tend to have systematically lower effective temperature (of up to 300 K) than field-age (from about 1 Gyr) objects of the same spectral type. This discrepancy is likely due to the fact that clouds start appearing in mid-L type brown dwarfs (more details in Section 1.1.3 and Chapter 5.2). The distinguishable features of the M-L-T-Y spectral classes are the following:

- **M type**: Cool red stars (starting from M7, brown dwarfs) with dominating molecular absorption bands, such as titanium oxide (TiO) and vanadium oxide (VO); still strong metal lines.
- **L type**: Cool dark-red brown dwarfs with strong molecular absorption bands of metal hydrides (CrH, FeH), water ($H_2O$), carbon oxide (CO), alkali metals (Na, K, Rb, Cs), and weakening TiO and VO.
- **T type**: Very cool infrared brown dwarfs with strong methane ($CH_4$) absorption but weakening CO bands.
- **Y type**: The coolest infrared brown dwarf with the appearance of ammonia ($NH_3$) absorption. Chapter 3.3 of my dissertation is dedicated to characterization of the spectral energy distribution of the coolest known Y dwarf to date.

### 1.1.2 Color-magnitude diagrams for brown dwarfs and directly imaged exoplanets

Due to their incapability to sustainably burn hydrogen-1 in their interiors, the evolution of brown dwarfs proceeds differently to the one of the main-sequence stars - brown dwarfs contract and cool down with time evolving to a later spectral type, which is not true for stars. Therefore, brown dwarfs are usually placed on separate H-R diagrams. Figure 1.1) clearly shows that brown dwarfs become fainter with later spectral type. Moreover, for most cases it can be stated that the spectral sequence is a temperature sequence (e.g., Kirkpatrick 2005), which means that a range of effective temperatures can be uniquely attributed to a certain spectral class. Some exceptions to this trend can be explained by dust clouds that are mainly present in young brown dwarfs (e.g., Filippazzo et al. 2015).

However, color-magnitude diagrams can be a convenient alternative to H-R diagrams because they do no require spectroscopic observations in order to locate an object on a plot. Moreover, color-magnitude diagrams for brown dwarfs clearly outline the important "L/T transition", where

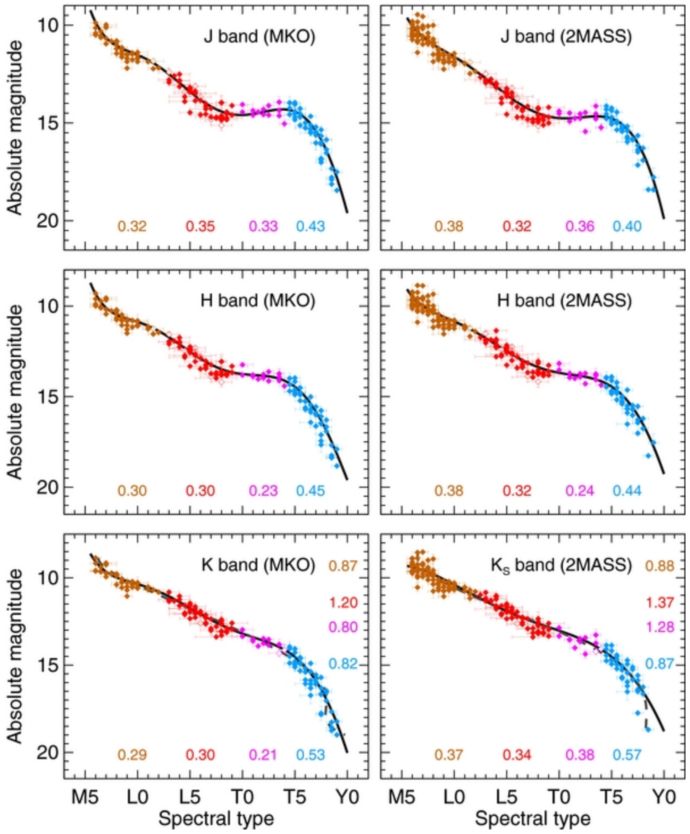

Figure 1.1: Near-infrared absolute magnitudes as a function of spectral type for brown dwarfs (Dupuy & Liu 2012). Solid black lines are polynomial fits to the data. Color-coded coefficients at the bottom of each panel are rms about the fit for each spectral range: M6–L2 (brown), L2.5–L9 (red), L9.5–T4 (purple), and ≥ T4.5 (blue).

hypothetically, clouds covering atmospheres of early-L dwarfs start to clear-out and disappear towards late-T dwarfs. It is accompanied by a blueward shift of ∼ 2 mag in $J - K$ and a slight increase in the brightness (see Figure 1.2). Color-magnitude diagrams are also convenient for detecting anomalies in individual objects. One of them is a sample of ultra-red brown dwarfs which color is normally attributed to dust enhancement or high metallicity (e.g., Leggett et al. 2007; Cushing et al. 2008; Marocco et al. 2014; Manjavacas et al. 2014).

Color-magnitude diagrams also make the connection between brown dwarfs and giant exoplanets more obvious. The high-contrast imaging instruments used over the past decade were able to detect planets that are only $10^6$–$10^7$ times fainter that their parent stars. Moreover, because of the angular resolution limit, only giant planets outside several tens of astronomical units could be directly resolved. Therefore, only the brightest planets at large separations could be characterized, which limited it to giant self-luminous young exoplanets that have not yet cooled down after formation. And since the influence of the flux from the host star is negligible for such

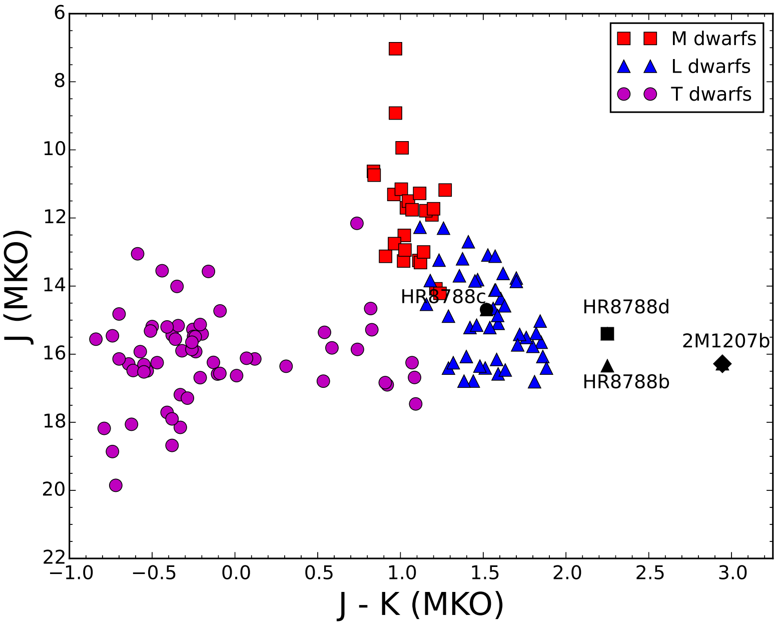

Figure 1.2: Color-magnitude diagram for some of the brown dwarfs and directly imaged exoplanets.

planets, they have properties (spectral class and photometric colors) similar to brown dwarfs of the same effective temperature. For instance, the HR8799bcde (Marois et al. 2008, 2010) system consists of four giant planets with masses of 5–10 $M_{Jup}$ and luminosities that are consistent with L/T-transition brown dwarfs. Additionally, a number of isolated free-floating objects of planetary mass ($< 13\ M_{Jup}$) have been discovered over the past few years (e.g., Gagné et al. 2014, 2015; Liu et al. 2013; Luhman 2014). These objects are attributed to late-T or Y spectral classes. On the other hand, both young brown dwarfs and giant exoplanets reveal similar spectral and photometric features, such as a triangular shape of the continuum in $H$ band caused by a decrease of $H_2$-collision-induced absorption (e.g., Patience et al. 2012), or redder colors in color-magnitude diagrams than “field” (i.e. old) brown dwarfs, plausibly pointing to enhanced dust content in their atmosphere. These special features may possibly be caused by low gravity in young brown dwarfs and giant exoplanets because, due to their youth, these objects have not finished contracting yet.

The similarities in observational features that are clearly seen in color-magnitude diagrams allow us to claim that young brown dwarfs can be considered as giant planet analogs (e.g., Faherty et al. 2014). The new-generation of high-contrast imaging instruments, such as SPHERE (Spectro-Polarimetric High-contrast Exoplanet REsearch) and GPI (Gemini Planet Imager) will allow us to detect fainter, hence lower-mass exoplanets closer-in to the star. In fact, the recent discovery using GPI, Eridani 51 b (Macintosh et al. 2015), is the lowest-mass (2 $M_{Jup}$) directly imaged exoplanet to date. Similar detections in the future will allow us to bridge the gap between lower-mass brown dwarfs and Jupiter-like planets.

### 1.1.3 Clouds in brown dwarfs and giant exoplanets

The photometric variability commonly seen in brown dwarfs is often attributed to rotational modulation of inhomogeneous cloud structures in their atmospheres. It is believed that at temperatures below 2600 K some refractory elements condense forming "dust" clouds in brown dwarf atmospheres (Burrows & Sharp 1999; Lodders 1999; Burrows et al. 2006). As dust clouds form and thicken, the spectral energy distributions of brown dwarfs become redder (from early- to mid-L spectral classes). However, at temperatures about 1200 K, clouds start to disappear transitioning to methane-rich cloud-free atmospheres ("L/T transition" in brown dwarfs from late-L to early-T classes).

Recently, several surveys have studied the variability in detail. The *Spitzer* large-scale survey by Metchev et al. (2015) revealed mid-infrared variability for up to a few percent in more than 50% of L- and T-type brown dwarfs. The *HST* SNAP survey by Buenzli et al. (2014) found that about 30% of L5–T6 brown dwarfs show variability trends. The described results from space telescope have been also confirmed by ground-based surveys (Radigan et al. 2014; Wilson et al. 2014). Apai et al. (2013) and Buenzli et al. (2015) found that the variability as a function of wavelength is reproduced better by a combination of thin and thick clouds, rather than by gaps in the cloud coverage.

Several years ago Luhman (2014) discovered the closest to the sun brown dwarf binary system WISE J104915.57-531906.1AB (hereafter, Luhman 16AB). Due to its proximity (≈ 2pc; Luhman & Esplin 2014), Luhman 16 AB can be studied in unprecedented detail and has become a benchmark sytem. A pioneering study by Crossfield et al. (2014) allowed to obtained the first Doppler map of B component in the brown dwarf binary system Luhman 16AB (WISE WISE J104915.57-531906.1AB). Doppler imaging exploits disturbances of the averaged spectral line profile of an object to identify (sub-)stellar surface inhomogeneities. Time-dependent spectral series allows us to detect changes in these inhomogeneities due to the object's rotation. Until now, this method was broadly used for stars to map the distribution of hot and cool spots in the chromosphere (examples of classical studies can be found in Vogt et al. 1987; Rice et al. 1989). Using Doppler imagingCrossfield et al. (2014) for the first time directly confirmed the inhomogeneity of the surface in Luhman 16B. This study was complimented by Biller et al. (2013) that attempted a multi-band ($r'$ $i'$ $z'$ JHK) photometric characterization of the system. The authors detected the phase offset between light curves of some of the photometric bands. Since different wavelength probe different atmospheric levels, the phase offset support a hypothesis that the photometric variability in Luhman 16B can be explained by combinations of thin and thick clouds in its atmosphere.

Recently, the photometric variability was discovered in planetary-mass object, both free-floating and orbiting a star. Biller et al. (2015) reported the photometric variability in a 5–10 $M_{Jup}$ (Liu et al. 2013) free-floating object. This was the first detection of variability in a planetary-mass object. Using high-dispersion spectroscopy, Snellen et al. (2014) were able to detect fast spin rotation in a directly imaged exoplanet for the first time. Most recently, Zhou et al. (2016) and Apai et al. (2016) presented photometric variability studies for directly imaged companions at the exoplanet/brown-dwarf mass boundary, using space- and ground-based observations, respectively. These new data allow us to assume that the rotationally modulated variability might be common for a wide range of giant exoplanets and brown dwarfs.

Beside the cloud architecture, the cloud composition is also of particular interest for brown dwarf studies. For instance, condensing refractory elements (silicates and iron) dominate L dwarf clouds, but these clouds dissipate at the L/T-transition. The variety of other condensates, such as Cr, MnS, $Na_2S$, ZnS, and KCl, are expected to form in cooler T dwarf atmospheres (Morley et al. 2012). Cooler Y dwarfs may even consist of water ice clouds (Morley et al. 2014). Chapter 3 of this dissertation is dedicated to constraining the presence of water ice clouds in the coolest known Y dwarf, WISE 0855-07. Currently, the question of if the inhomogeneity of water ice clouds remains open, and is expected to be addressed with future generation instruments (such as JWST, or E-ELT) that will have a much higher sensitivity.

It should also been mentioned that recently an alternative theory, that does not employ clouds, has been proposed. Tremblin et al. (2015, 2016) argue that cloud models cannot reproduce a number of observed features in brown dwarfs, such as the $J$-band brightening blueward the L/T-transition, or absorption features at 10 $mu$m. Additionally, clouds in brown dwarfs are expected to produce a polarization signal that, however, has not been detected so far (e.g., Goldman et al. 2009). Therefore, Tremblin et al. (2015, 2016) developed an alternative theory that implement fingering double diffusive convection similar to that present in the Earth's oceans. But in case of brown dwarfs, chemical reactions themselves play the role otherwise played by molecular diffusion, and lead to thermo-chemical instability. Tremblin et al. (2015) have shown that spectra of T and Y dwarfs can be reproduced with the cloudless model if accounting for non-equilibrium chemistry of $NH_3$. However, these models still do not explain the periodic photometric variability in brown dwarfs and do no suggest stronger observational predictions than cloudy models. Therefore, in this thesis to the theory with cloudy brown dwarfs atmospheres.

## 1.2 Chemical abundances as a key to formation scenario of very low-mass companions

Several studies (e.g., Valenti & Fischer 2005; Johnson & Apps 2009; Johnson et al. 2010; Mayor et al. 2011) have shown that giant exoplanets occur more often around higher-metallicity stars. This could be an outcome of the core accretion formation theory where massive gaseous planets are formed in disks by runaway gas accretion onto cores. The larger the metallicity of the disk, the faster the core is formed and more gas can be accreted onto it. On the other hand, lower-mass planets do not accrete large amounts of gas over the timescale of core formation, and therefore, they are less sensitive to the disk metallicity (Mordasini et al. 2012).

Another important parameter that could be used as a key to companion formation is the C/O ratio. As noted in Öberg et al. (2011), due to different condensation temperatures of water, carbon oxide, and carbon dioxide, the icelines for these molecules are located at different part of the protoplanetary disk (Fig. 1.3) . This leads to different amounts of gaseous carbon and oxygen throughout the disk. Therefore, the C/O ratio of a companion formed by core accretion can vary and will reflect that of the part of the disk where it formed. Conversely, companions formed by disk gravitational instability are expected to have C/O ratios consistent with their host stars. This is because the material from which they formed is well-mixed and represents the average chemical abundance of the disk. This abundance is the same as the host star, since they formed from the same cloud.

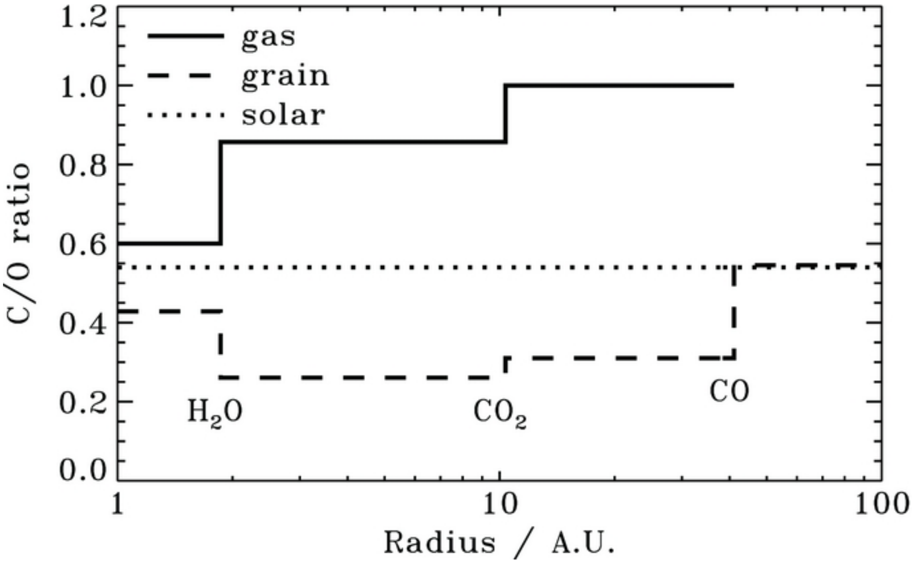

Figure 1.3: C/O ration within a protoplanetary disk around a solar-like star (Öberg et al. 2011).

Several other studies explored the range of C/O ratios that planets formed by core accretion may have. Helling et al. (2014), in contrast to Öberg et al. (2011), provide more detailed analysis of gas and ice abundances in a pre-stellar core and a protoplanetary disk, and however, provide a similar range of possible C/O ratios. Thiabaud et al. (2014, 2015), Marboeuf et al. (2014b,a), and Cridland et al. (2016) have attempted to incorporate the formation process when modelling final abundances in exoplanets. Most recently, Mordasini et al. (2016; subm.) have created a model CHAIN that includes the simulation of planets via core accretion, the planets' evolution and possible migration within the disk, the solution for the planetary inner structure, the chemical model, and various instrument profiles. By linking all these modelling processes the authors are able to obtain instrument-specific synthetic spectra for a planet with a certain formation and evolution history given a protoplanetary disk chemical model.

In Chapter 4, I attempt to determine abundances for both the companion and the host star in the AB Pic system, and discuss the feasibility to distinguish between different formation scenarios for the companion based on the obtained results. I also present the novel method for fitting models to observed spectra, that allows to account for possible systematic effects.

## 1.3 Methods of characterization of (sub-)stellar atmospheres

All the approaches to characterize atmospheres of stars, brown dwarfs, and exoplanets are model-dependent in smaller or bigger degree. It means that all the methods make assumptions about pressure-temperature profiles, convection, and spectral line strengths based on analytical calculations, computer simulations, and laboratory experiments (to determine opacities of certain elements).

Traditionally, the forward modelling approach is used where models are calculated for each set of parameters - by determining a pressure-temperature profile and then running a radiative transfer routine to calculate synthetic spectra. Simulated spectra then compared to observations, and parameters of the best-matching model are assigned to the object of interest.

The main advantages of forward modelling is that this method is physically self-consistent. However, it is computationally expensive, especially when trying to avoid the sparsity in the parameter grid. Nevertheless, over the past decades, due to growing computational capacities, atmosphere modeling has been experiencing a boost. Special attention was given to creation of models for the lower temperature (< 2600 K) regime. The challenge for such models is that at lower temperatures multiple species condense to form clouds. At temperatures from 2600 K to 1300 K (late M, L, and early T dwarfs) some refractory materials (iron, corundum, silicates) condense, forming clouds (Lunine et al. 1986; Fegley & Lodders 1996; Burrows & Sharp 1999; Lodders &

Fegley 2002, 2006; Lodders 2003; Helling & Woitke 2006; Visscher et al. 2010). These clouds clear over the small range of effective temperatures around 1200-1300 K (early T dwarfs), and the methane features become prominent in the near-infrared. However, some sulfide and salts start condensing at this temperature range (Lodders 1999). For instance, the warmest Y dwarfs (500–600 K) consist of condensed $Na_2S$ salts (Morley et al. 2012). As temperatures go even lower (Y dwarfs), ammonia features start to appear (Burrows et al. 2003). And at temperatures lower than 300 K, Y dwarfs are predicted to have water ice clouds (Visscher et al. 2006; Morley et al. 2014).

Nowadays, multiple independent groups have developed their own atmospheric models that consider the lowest temperature regime. One of the commonly-used models is BTSettl (Allard et al. 2013). These models use line-by-line opacities that take into account the effect of atomic and molecular absorbers (Allard et al. 2003). The BTSettl models implement a one-dimensional radiative transfer code PHOENIX to calculate synthetic spectra for each set of parameters. These models take into account the effect of condensing clouds in (sub)-stellar atmospheres, which occurs at < 2600 K. However, these models do not treat the effects of water clouds.

The first models that incorporate water ice clouds were published by Burrows et al. (2003). However, these models do not find strong effects in the atmosphere introduced by water clouds. The most recent models that taking into account condensed water clouds were presented by Morley et al. (2014). These models contain self-consistent physics and chemistry. The opacity database unites results of laboratory experiment, as well as quantum mechanics calculations (Freedman et al. 2008). These opacities are updated with the new ammonia opacity list (Yurchenko et al. 2011) and an improved treatment of the pressure-induced opacity of $H_2$ collisions (Richard et al. 2012). The cloud code implemented in the models follows the approach of Ackerman & Marley (2001) and has been upgraded for the effects of the presence of the water ice clouds.

The described models were used during the work in this dissertation. However, I leave out a number of other widely-used atmospheric models (e.g., Sudarsky et al. 2003; Helling et al. 2008), which are beyond the scope of this thesis. Additionally, new-generation models that use additional parameter dimensions have recently appeared - Mollière et al. (2015) study the influence of stellar parameters, different metallicities and C/O ratios on spectra of hot Jupiters. The current version of the models does not yet implement the cloud physics. However, for directly imaged exoplanets and brown dwarfs, the stellar flux can be neglected but the effects of the cloud presence should be taken into account. Therefore, the models by Mollière et al. are not used in this dissertation.

## 1.4 Main problematics and thesis outline

Using photometric and spectroscopic observations, we are able infer key physical parameters for exoplanets, brown dwarfs, and very low-mass stars. By applying models, we can determine effective temperature, radius, chemical abundances, a potential cloud structure for these objects. In its turn, chemical abundances can provide us with crucial information for understanding of formation and evolution of sub-stellar companions. However, since the parameters are model-dependent, the interpretation of results must be vey critically, and models should be carefully selected preferably tested.

Therefore, in **Chapter 2** of my dissertation I present a benchmark star sequence for testing stellar and atmospheric models. The "single-star" sequence of the Hyades was compiled using literature and my own observations. By excluding binary and multiple systems from the list of the Hyades member, I was able to reduce the scatter in the color-magnitude diagram, and therefore to provide a fiducial sequence that can be compared with theoretical isochrones.

In **Chapter 3**, I perform a model-dependent characterization of the coolest known Y dwarfs, WISE 0855-07 and try constrain the presence of water ice clouds in its atmosphere. I show that none of the available atmospheric models can described the observations completely, giving another example of how model-dependent interpretation can be limited.

In **Chapter 4**, I attempt to characterize the AB Pic A+B system, in order to understand the formation history of B component. I derive parameters for A companent in a classical way by comparing with model prediction, but B component I create a novel fitting method. This method allows to account for systematic effects introduce by models and/or observations. After fixing the systematics, I estimate a C/O ration in AB Pic B and speculate about its formation.

In conclusion, I discuss the future development of characterization of sub-stellar objects. I discuss the way of cloud parametrization in models, as well as data-driven and machine-learning approaches for determining physical parameters.

# Chapter 2

# The Hyades single-star sequence for testing stellar and atmospheric models

This chapter is based on Kopytova et al. (2016), for which I led data analysis and comparison with theoretical models for the interpretation, compilation of literature data. I also led the scientific discussion and made main conclusions.

## 2.1 Introduction

The knowledge of physical parameters of stellar and substellar objects provides the basis for astrophysics. Observations allow us to determine distance (using parallaxes), age (through membership in clusters or moving groups), mass (by calculating orbital parameters in binary systems), and radius (in transiting and eclipsing systems). Asteroseismic scaling relations can also provide estimates for stellar mass and radius. However, these relations may suffer from unknown systematic effects and may require additional calibration using observations and theoretical models (e.g., Miglio et al. 2012; Douglas et al. 2016). Therefore, when dealing with isolated stellar objects, we usually have to rely on theoretical models to determine mass and age. While stellar and atmospheric models are rapidly evolving, we need a powerful tool to test and calibrate them. Open clusters are good candidates for this role, since they contain many coeval objects of the same chemical composition spanning a range of masses, thus avoiding the problems of small number statistics. Additionally, open clusters have distance and age estimates that are independent of theoretical models to be tested.

In general, the validation of theoretical models consists of two independent problems - one is testing interior structures of stars, the other is inspecting atmospheric models. However, this process is non-trivial because models of the interior structure provide us with physical parameters (e.g., effective temperature, luminosity, mass, and age) that need to be converted into observed quantities (magnitudes, colors, and fluxes). This conversion exploits grids of synthetic spectra provided by atmospheric models and requires careful calibration for specific photometric bands (e.g., Da Rio & Robberto 2012).

In the past, open clusters had already been used as benchmarks for theoretical models. Bell et al. (2012) used the Pleiades to test existing pre-main-sequence isochrones by comparing their predictions with well-calibrated color-magnitude diagrams in the wavelength range of 0.4–2.5 $\mu$m. Bell et al. have shown that no pre-main-sequence model can describe the observed Pleiades sequence for the temperatures cooler than 4000 K. The predicted fluxes are overestimated by a factor of 2 at 0.5 $\mu$m, with the difference decreasing with increasing wavelength.

In comparison to the Pleiades (d ~ 120–140 pc; Percival et al. 2005; van Leeuwen 2009), the Hyades open cluster is closer to the Sun (d ~ 45 pc; Perryman et al. 1998; van Leeuwen 2009). This allows us to resolve companions with smaller physical separations, and also to analyze less luminous, hence less massive, objects. Moreover, Röser et al. (2011) reported 724 likely members of the Hyades, with individual kinematic distance estimates using the convergent point method (e.g. van Leeuwen 2009). Individual distance measurements allow us to get more precise absolute magnitudes for each member of the Hyades. The previous attempt to test stellar models with the Hyades (Castellani et al. 2001) showed a discrepancy between theoretical predictions and the observed main-sequence sample, especially at the region of the coolest stars.

In this chapter, I present a fiducial "single-star sequence" in the Hyades based on literature data and my own AstraLux Lucky Imaging observations. Furthermore, I use the obtained sequence to provide a test for commonly used stellar and atmospheric models.

## 2.2 Observations and literature data

To test interior and atmospheric models I use $JHK_s$ 2MASS data (Skrutskie et al. 2006), which provides a homogenous photometric set for all the 724 possible members of the Hyades. The angular resolution of 2MASS is limited to $\sim 3''$. To avoid a scatter on color-magnitude diagrams that can be introduced by unresolved binary and multiple systems, or optical blends with unrelated field or background stars, I check the literature and archived databases for multiplicity and perform Lucky Imaging observations. The saturation threshold of the 2MASS photometry is $K_s \sim 4$ mag; therefore, fluxes for the brightest stars are replaced by the data from Carney (1982), with a transformation to the 2MASS system applied. The color uncertainties are calculated in the standard way exploiting independent photometric magnitude uncertainties estimates.

### 2.2.1 Literature data

I check previous studies that make an attempt to identify binary and multiple systems in the Hyades including works of Patience et al. (1998), Mermilliod et al. (2009), Morzinski (2011), and Duchêne et al. (2013) and archival data from Hipparcos, Hubble Space Telescope (HST), and Washington Double Star (WDS; Mason et al. 2001) catalogs. The HST data have also been previously studied by Gizis & Reid (1995), Reid & Gizis (1997), and Reid & Mahoney (2000). Characteristics of the surveys are summarized in Table 2.1.

### 2.2.2 AstraLux Lucky imaging observations

The Lucky Imaging technique is based on a series of short (few to several 10 ms) exposures, which "freeze" the speckle clouds caused by atmospheric turbulence. The series of frames is sorted by the best quality (based on the brightest pixel), and typically the best 1% to 10% of the images are shifted and co-added, resulting in a close to diffraction limited image. AstraLux Norte is a lucky imaging camera mounted on the 2.2m telescope at the Calar Alto observatory in Spain (Hormuth et al. 2008). The camera has a field of view (FOV) of $24'' \times 24''$ and a pixel scale of $\sim$ 47 mas/px.

The observations were performed in November 2011, and November and December 2012. Depending on the brightness of the target and observing conditions, either a 15 or 30 ms exposure time was chosen, so that 20,000 or 10,000 short exposures were obtained for each target, respectively. Only one quadrant of the detector was read-out to facilitate shorter integration times.

The Hyades targets for the AstraLux run are pre-selected based on the results of the literature and archive check. In total 198 Hyades members are observed in SDSS $i'$ and $z'$ filters. The analysis for each target is performed based on the best 1% frames that are co-added together. Possible companions are identified by a visual check of each co-added frame (see Fig. 2.1) resulting in 40 Hyades members that reveal one or several companion candidates. Twenty-eight of the 40 systems with companion candidates did not have any binary/multiplicity record in previously published surveys. Most of the AstraLux candidates to binary and multiple systems have only one epoch of observations, therefore they cannot be confirmed as common proper motion companions. Non-detections exclude companions outside a projected separation of 3–7 AU (depending on the distance to a star), though these stars could still have unresolved companions

| Survey | Telescope | Method | Angular Resolution | Observed | Binary/Multiple |
|---|---|---|---|---|---|
| Patience et al. (1998) | 5m Hale telescope<br>Palomar observatory | 2.2 $\mu$m<br>speckle imaging | 0.″11 | 163 | 33 |
| Mermilliod et al. (2009) | Swiss 1m telescope<br>Haute-Provence Observatory | CORAVEL<br>spectroscopy | - | 139 | 25 |
| Morzinski (2011) | Keck and Lick<br>observatories | Adaptive<br>optics | 0.″06 | 75 | 30 |
| Duchêne et al. (2013) | Keck II | Adaptive<br>optics | 0.″06 | 9 | 5 |
| HST | Hubble Space<br>Telescope | Imaging | 0.″05 | 57 | 8 |
| Hipparcos catalogue | Hipparcos Space<br>Mission | Imaging | 0.″10 | 195 | 22 |
| AstraLux Norte | 2.2m telescope<br>Calar Alto observatory | Lucky<br>imaging | 0.″11 | 198 | 40 |

Table 2.1: Characteristics of various multiplicity surveys in the Hyades. Some stars were studied by several surveys. The WDS catalog is not presented in the table because its instrument characteristics is inhomogeneous.

closer in.

In total 463 Hyades members are observed in one or more surveys and 213 of them are identified as candidates for binary or multiple systems leading to 250 stars that do not have identified companions outside projected separation of 2–7 AU (depending on survey and distance to the star). Importantly, the angular resolution of instruments in the surveys we use varies from $0\farcs05$ to $0\farcs11$, which, in addition to various stars' distances, gives a range of separation where companions can be detected (2–7 AU; see Table 2). Hence, this means different detection thresholds for companions depending on the survey(s) in which the system was observed. Since this complicates the statistical analysis for constraining the number of binary and multiple systems, a robust estimate of the multiplicity properties of the Hyades will be a subject of a separate paper.

The Hyades targets for the AstraLux run are pre-selected based on the results of the literature and archive check. In total 198 Hyades members are observed in SDSS $i'$ and $z'$ filters. The analysis for each target is performed based on the best 1% frames that are co-added together. Possible companions are identified by a visual check of each co-added frame (see Fig. 2.1) resulting in 40 Hyades members that reveal one or several companion candidates. Twenty-eight of the 40 systems with companion candidates did not have any binary/multiplicity record in previously published surveys. Most of the AstraLux candidates to binary and multiple systems have only one epoch of observations, therefore they cannot be confirmed as common proper motion companions. Non-detections exclude companions outside a projected separation of 3–7 AU (depending on the distance to a star), though these stars could still have unresolved companions closer in.

In total 463 Hyades members are observed in one or more surveys and 213 of them are identified as candidates for binary or multiple systems leading to 250 stars that do not have identified companions outside projected separation of 2–7 AU (depending on survey and distance to the star). Importantly, the angular resolution of instruments in the surveys we use varies from $0\farcs05$ to $0\farcs11$, which, in addition to various stars' distances, gives a range of separation where companions can be detected (2–7 AU; see Table 2). Hence, this means different detection thresholds for companions depending on the survey(s) in which the system was observed. Since this complicates the statistical analysis for constraining the number of binary and multiple systems, a robust estimate of the multiplicity properties of the Hyades will be a subject of a separate paper.

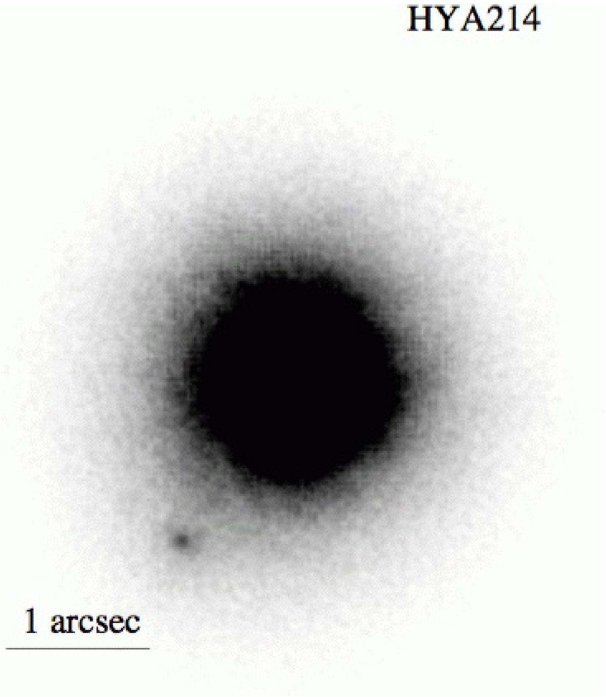

Figure 2.1: AstraLux Norte $z'$-band image of a binary candidate in the Hyades. The image is shown in log scale.

## 2.3 Models

In this section we describe the stellar evolutionary models and synthetic spectra used to produce theoretical isochrones for the Hyades and compare them with the observed single-star sequence.

### 2.3.1 Interior models

We use two different stellar interior models - DARTMOUTH and the new PISA grids produced for the Hyades case. More recently, new BHAC15 (Baraffe et al. 2015) stellar models have been published. These models follow the widely used BCAH98 models (Baraffe et al. 1998). However, BHAC15 models do not provide interior structures for super-solar metallicities yet, therefore, we do not use them for isochrone comparison.

The Dartmouth Stellar Evolution Program (DSEP) (Dotter et al. 2008) is a family of stellar evolutionary models exploring a wide range of metallicities and $\alpha$-enhancements. The basic equation of state for tracks $M \geq 0.8 M_{\odot}$ is a general ideal gas EOS with a Debye-Hückel correction (Chaboyer & Kim 1995). The FreeEOS in the EOS4 configuration is used for the lower mass tracks. Evolutionary tracks are computed for masses from 0.1 to 4 $M_{\odot}$. We use isochrones for [Fe/H] = 0.14 and [$\alpha$/H] = 0.0. For the Hyades metallicity, the DSEP models include a convective core overshooting parameter of 0.2 times the pressure scale height for M ≥ 1.1 $\mathrm{M}_{\odot}$.

The new PISA models have been computed by means of the FRANEC stellar evolutionary code (Degl'Innocenti et al. 2008), adopting input physics similar to the parameters already discussed in Tognelli et al. (2011) and Dell'Omodarme et al. (2012). The main difference with respect to the models already available at the Pisa database page[1] is the adoption of the SCVH95 EOS for the computation of stellar models with mass lower than 0.2 $M_{\odot}$. We adopt the recent Asplund et al. (2009) solar metal distribution, and the corresponding mixing length parameter calibrated on the Sun, namely $\alpha_{\mathrm{ML}} = 1.74$. We also include a mild convective core overshooting ($\beta_{\mathrm{ov}} = 0.2$) for M ≥ 1.2 $\mathrm{M}_{\odot}$ (Tognelli et al. 2012). The models have been computed in the mass range [0.1, 2.8] $\mathrm{M}_{\odot}$ from the early pre-MS evolution up to the exhaustion of the central hydrogen. The corresponding isochrones in the age interval [400, 800] Myr, with an age spacing of 10 Myr, have been generated. The stellar models have been computed for [Fe/H] = +0.14, which – adopting the Asplund et al. $(Z/X)_{\odot} = 0.0181$ and $\Delta Y/\Delta Z = 2$ (Casagrande 2007) – corresponds to $Y = 0.283$ and $Z = 0.0175$.

To obtain a consistent set of magnitudes for both the Dartmouth and Pisa models, we transform the theoretical isochrones from the ($\log T_{eff}$, $\log L/L_{\odot}$) plane into the color-magnitude diagram by means of our own calculation of the photometric band. To do this we use synthetic spectra obtained from detailed atmospheric models following the method described in Section 2.3.3.

### 2.3.2 Atmospheric models

To calculate synthetic photometry we use synthetic spectra provided by BT-Settl atmospheric models (Allard et al. 2013). The BT-Settl models take into account gravitational dust settling in atmospheres of objects at temperatures below ~2600 K, following the approach described in Rossow (1978). Opacities are introduced line by line to account for the effect of molecular absorbers, as described in Allard et al. (2003). The synthetic spectra are calculated using the radiative transfer model atmosphere code PHOENIX that implements static and radial (1D) approximations (Allard et al. 2001). We apply the latest publicly available release of BT-Settl (last update in March 2015) that uses the Caffau et al. (2011) solar abundances. For effective temperatures $T_{eff} < 7000$ K we use the BT-Settl 2010 version, which exploits the solar abundances of Asplund et al. (2009).

---

[1] `http://astro.df.unipi.it/stellar-models/`

### 2.3.3 Synthetic photometry with TA-DA

The Tool for Astrophysical Data Analysis (TA-DA; Da Rio & Robberto 2012) is an interactive software that allows stellar photometric data to be analyzed in comparison with theoretical models and stellar parameters to be derived using multi-band photometry. TA-DA is able to interpolate stellar interior models and to produce synthetic photometry by converting stellar parameters into photometric magnitudes in given filters using grids of synthetic spectra. The conversion is done in the standard way, by integrating the synthetic spectra over the filter bandwidths and normalizing onto a spectrum of Vega. Therefore, TA-DA is very suitable for combining various stellar interior and atmospheric models to derive photometric magnitudes for different evolutionary tracks and isochrones. We use stellar interior models and synthetic spectra from grids of atmospheric models to obtain various isochrones for the Hyades with TA-DA.

## 2.4 Hyades single-star sequence

In this section, we give the Hyades single-star sequence as an example to test the theoretical models. Additionally, we determine stellar parameters of the sequence members by comparing photometric observations to the calculated model isochrones. Absolute $JHKs$ magnitudes for the stars on the single-star sequences (see Table 2) are derived from the distance estimates in Röser et al. (2011) and the available near-infrared (NIR) photometry. For all stars we assume the NIR foreground extinction to be negligible.

### 2.4.1 Isochrone comparison

We compute theoretical isochrones for combinations of BT-Settl 2010 atmospheric models with PISA and DARTMOUTH interior models for the age of 630 Myr, which is close to the 625±50 Myr estimate of Perryman et al. (1998). We place the obtained isochrones on $J$ vs. $J - K_s$, $J$ vs. $J - H$, and $K_s$ vs. $H - K_s$ color-magnitude diagrams together with the observed single-star sequence of the Hyades. As can be seen, PISA and DARTMOUTH tracks both predict the observed sequence reasonably well, even the behavior of the "knee-shaped" part, around $\sim 0.6 M_\odot$ which was problematic as was previously shown by Röser et al. (2011) for older generation evolutionary models. The PISA models are available with ($\beta = 0.2$) and without convective core overshooting. Both sets of models are in good agreement with the presented data, the only difference being the inferred cluster age. As expected, the inclusion of convective core overshooting leads to older ages. Adopting $\beta = 0.2$, the best fitting isochrone provides an age of 630 Myr, whereas isochrones without core overshooting give 550 Myr.

The observed sequence reveals a larger scatter towards lower masses, because the faintness of the objects causes larger errors in the photometric and kinematic measurements. Additionally, a small (~0.05 mag) systematic offset can be noted in the $J$ vs. $J - K_s$ and $K_s$ vs $H - K_s$ diagrams – the observed sequence shifted to redder colors than the theoretical predictions.

### 2.4.2 Physical parameters of single stars with TA-DA

TA-DA (see Section 2.3.3) includes an option that gives theoretical predictions for stellar parameters based on a comparison of synthetic photometry with observed photometric magnitudes. The dimension of the observational space (number of colors or magnitudes) must be greater than or equal to the number of free parameters given by stellar interior models. The TA-DA parameter filter is described in Da Rio & Robberto (2012) and performs a multiband least-square fit. TA-DA also allows the estimation uncertainties for derived stellar parameters using a Monte Carlo simulation, in which the photometry is displaced according to photometric errors.

Using TA-DA we derive theoretical stellar parameters for 250 members of the Hyades single-star sequence (see Table 2) using BT-Settl2010+PISA isochrones for [Fe/H]=+0.14.

### 2.4.3 Spectral energy distribution from X-ray to mid-infrared

For all stars in the single star sequence, we compiled the available literature data from X-rays to mid-infrared ROSAT X-ray (Stern et al. 1995), GALEX UV (Martin & GALEX Team 2005), APASS $gri$ (Henden et al. 2015), 2MASS $JHK_s$, and WISE $W1$ to $W4$, and computed absolute fluxes and magnitudes based on the parallaxes from Röser et al. (2011). The values are provided in long electronic version of Table 2.

## 2.5 Summary and future prospects

Using previously published high angular resolution and spectroscopic studies and our own Lucky Imaging AstraLux Norte observations, we compiled a “single-star sequence” for the Hyades, which at an average distance of 45 pc is the open cluster closest to the Sun. In total, we identified 250 members of the cluster that do not show signatures of a companion outside the 2–7 AU projected separation (depending on the distance to each individual member and the survey).

Comparison of the near-infrared properties of the single-star sequence with theoretical isochrones based on the PISA and DARTMOUTH stellar interior models and BT-Settl 2010 atmospheric

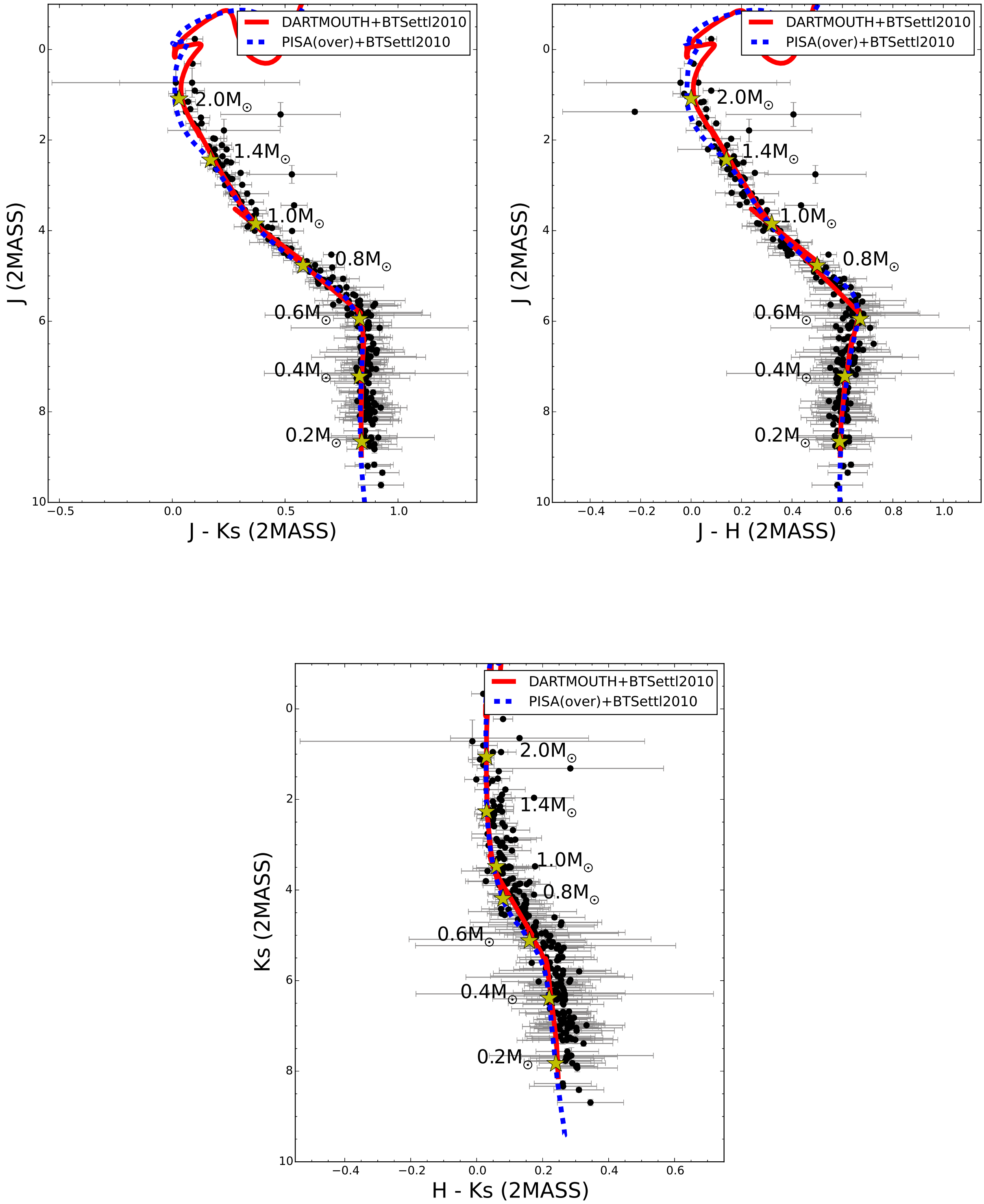

Figure 2.2: $J$ vs $J - K_s$ (top left panel), $J$ vs. $J - H$ (top right panel) and $K_s$ vs. $H - K_s$ (bottom right panel) color-magnitude diagrams. The Hyades observed single-star sequence is over-plotted with theoretical isochrones (630 Myr) from different evolutionary models - PISA (dashed blue line) and DARTMOUTH (solid red line). Synthetic photometry for isochrones are calculated in TA-DA using BT-Settl 2010 synthetic spectra.

models shows an overall good agreement for the mass range 0.13–2.30 M⊙. The only disagreement between models and observations is that for masses below 0.6 Msun the observed $J - K_s$ and $H - K_s$ colors are systematically redder than the isochrones by 0.05 mag. Despite these differences, the isochrones calculated using the most recent interior and atmospheric models, show a significantly better agreement with observations than isochrones produced by older generation models. The improvement can be particularly seen around 0.6–0.8 M⊙, where new isochrones are able to reproduce the knee-shaped part of the observed sequence.

We also estimate physical parameters (mass,effective temperature, and surface gravity) for the Hyades single-star sequence members based on theoretical predictions of combined PISA interior and BT-Settl 2010 atmospheric models.

The presented study has already served its scientific purpose. The Hyades single-star sequence was used by Douglas et al. (2016) to exclude possible binary and multiple systems from their sample. Douglas et al. report the dearth of rapid rotators among the Hyads with masses $\geq 0.3 M_{\odot}$However, the empirical gyrochronological relations are calibrated in such a way that for the age of the Hyades (600–650 Myr), the rotational break down should only occur at $0.6 M_{\odot}$ (e.g. Barnes 2003). This result might indicate that the magnetic braking mechanism is more effective than previously assumed.

The resulting single-star sequence can be used to test other various theoretical models and also to select candidates to search for close, previously unresolved binaries using spectroscopy and high-resolution imaging instruments. In the near future, results from the Gaia survey will provide us with kinematic, photometric, and spectroscopic information that will help to reduce the scatter at the lowest mass part of the observed sequence, which will enable us to test theoretical models with stronger confidence.

# Chapter 3

# Water ice clouds in the coolest Y dwarf

This chapter is based on Kopytova et al. (2014). I led the project from the very beginning, starting from an observing proposal. I completed data reduction and analysis myself, and led the discussion of results.

## 3.1 Introduction

Y dwarfs are substellar objects located at the coolest and lowest-mass edge of the brown dwarf M-L-T-Y spectral sequence (Kirkpatrick et al. 2012and ref. therein). Previous studies of Y0-1 spectral type objects reveal effective temperatures of 400–500 K and masses of 10–30 $M_{Jup}$ (e.g. Cushing et al. 2011; Dupuy & Kraus 2013; Leggett et al. 2013). Models predict a distinct atmospheric chemistry for Y dwarfs: $NH_3$ becomes apparent in the near-infrared and various species condense to form clouds (Burrows et al. 2003). In the warmest Y dwarfs these clouds are composed of $Na_2S$ (Morley et al. 2012), but at temperatures lower than 300 K the clouds may include $H_2O$, $NH_3$, and other, more exotic species (Burrows et al. 2003; Visscher et al. 2006; Morley et al. 2014).

Most recently, Luhman (2014) announced the detection of WISE J085510.83-071442.5 (hereafter, WISE 0855-07), a Y dwarf with $T_{eff} = 235 - 260$ K at a distance of 2.31±0.08 pc (Luhman & Esplin 2014), making it the fourth closest known stellar or brown dwarf system. WISE 0855-07 is the coolest Y dwarf known to date. Occupying a temperature regime intermediate between hotter and more massive L and T dwarfs ($T_{eff} > 550$ K) and Jupiter ($T_{eff} = 126$ K; e.g. Li et al.

2012), WISE 0855-07 provides a unique opportunity to test the presence of water clouds in the atmospheres of Y dwarfs at temperatures below 400 K.

Luhman (2014) and Wright et al. (2014) report observations of WISE 0855-07 from WISE (Wright et al. 2010), Spitzer, and ground-based facilities. However, the object is only detected by WISE and Spitzer in essentially two bandpasses at 3.6 $\mu$m and 4.5 $\mu$m. Beamín et al. (2014) also report a non-detection at $Y$ band giving an upper limit of $Y > 24.4$ mag at the $3\sigma$-level. On the other hand, Faherty et al. (2014) announce a $2.6\sigma$-detection of WISE 0855-07 giving $J3 = 24.8^{+0.53}_{-0.35}(J_{MKO} = 25.0^{+0.53}_{-0.35})$, or equivalently an upper limit of $J3 > 23.8$ mag ($J_{MKO} > 24.0$ mag) at $5\sigma$. Faherty et al. compare these observations with chemical equilibrium atmospheric models and demonstrate that WISE 0855-07 is $2.7\sigma$ from cloudless atmosphere models and can be reproduced by partly cloudy models (50%) containing sulfide and water ice clouds. However, the latter have been disputed by Luhman & Esplin (2014) who find that the SED of WISE 0855-07 can be explained by cloudless models that implement non-equlibrium chemistry. Nevertheless, we show that none of the available models that implement water clouds match all the existing observations completely (see Section 3), emphasizing that theoretical predictions for Y dwarf atmospheres are still quite uncertain. Obtaining a complete SED for WISE 0855-07 is essential for understanding atmospheric properties in the temperature regime below 400 K. In this paper, we present deep $z$-band observations of WISE 0855-07, determine its upper-brightness limit from our non-detection and discuss how our result constrains this object's atmospheric properties.

## 3.2 Observations and data analysis

Observations of WISE 0855-07 were carried out on May 31, 2014 using FORS2 mounted on VLT/UT1 at the ESO/Paranal observatory in Chile. FORS2 is a visual and near-UV focal reducer and low-dispersion spectrograph (Appenzeller et al. 1998). Observation were obtained in imaging mode using the red-optimized CCD through the z_GUNN+78 filter ($\lambda_0$=910 nm, FWHM=130.5 nm) with the high resolution collimator that gives a field of view of $4\rlap{.}'2 \times 4\rlap{.}'2$. Pixels were binned (2×2) resulting in a pixel scale of $0\rlap{.}''125$/pixel. In total, six images with an exposure time of 480 s each were taken. The telescope was pointed so that the predicted position of WISE 0855-07 was located on the upper chip of FORS2 which has a better sensitivity. A small telescope offset was applied after each integration, to avoid bad pixels and cosmic ray contamination.

All six frames were reduced in the standard manner using IRAF[1] (Tody 1993) - bias subtraction,

---

[1] IRAF is distributed by the National Optical Astronomy Observatories, which are operated by the Association of Universities for Research in Astronomy, Inc., under cooperative agreement with the National Science Foundation.

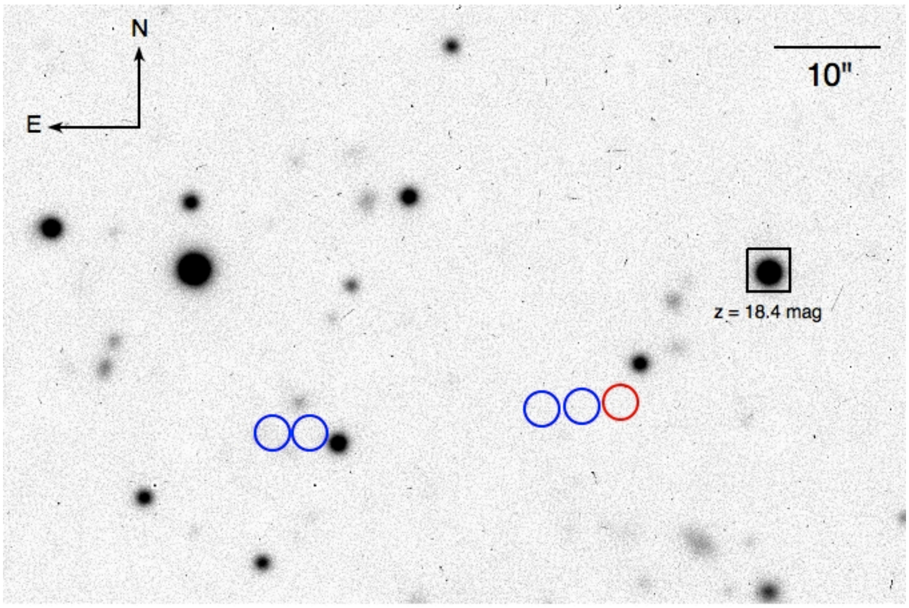

Figure 3.1: $z$-band FORS2 observations of the field containing WISE0855-07. Blue circles are WISE positions in 2010.34 and 2010.86 (the pair on the left) and Spitzer positions 2013.47 and 2014.05 (the pair on the right). The red circle is the expected position of WISE 0855-07 on May 31, 2014. No counterpart to WISE 0855-07 is detected in our $z$-band FORS2 frames. For reference, the square indicates a source with $z$(AB)=18.4 mag.

flat-fielding, fringe correction and sky subtraction. The reduced frames were aligned and co-added, in order to obtain a higher signal-to-noise. Astrometry and photometry from the Pan-STARRS1 (PS1) catalog (Schlafly et al. 2012; Tonry et al. 2012; Magnier et al. 2013) were used to measure the world coordinate system and to provide flux calibrations for the combined image. We used the method of Finkbeiner et al. 2014 (submitted to ApJ) to transform $z_{PS1}$ to the standard $z_{SDSS}$. Due to the lack of standard stars with z_GUNN+78 measurements, we cannot apply a proper transformation between z_GUNN+78 and $z_{SDSS}$ magnitudes. However, we apply the filter responses of the $z$_GUNN+78[2] and $z_{SDSS}$ filters to theoretical spectra (Burrows et al. 2003; Morley et al. 2014see Section 3) and find that the resulting flux varies at most ±0.05 mag from filter to filter. Hence, the uncertainty in the magnitude system cannot account for the differences between the observed data and the models (see Section 3).

We used IRAF/DAOFIND to search for a counterpart to WISE 0855-07. DAOFIND approximates a stellar point spread function with an elliptical Gaussian function. DAOFIND identifies no counterpart to WISE 0855-07 at its expected position in our z-band frames (Fig. 3.1). To place an upper limit on the z-band magnitude of the brown dwarf, we estimate the sky brightness and the sky standard deviation at this expected position. Using the calibrated photometry from PS1,

---

[2] Available through the FORS2 Exposure Time Calculator at `http://www.eso.org/observing/etc/`

we estimate an upper brightness limit for WISE 0855-07 of $z_{AB} > 24.8$ mag, or $F_\nu < 0.45\mu$Jy with $3\sigma$-confidence (corresponding to a direct measurement and uncertainty of $0.06 \pm 0.13\mu$Jy). This result is consistent with the non-detection of WISE 0855-07 in the $Y$-band using HAWK-I on UT4/VLT at the Paranal observatory by (Beamín et al. 2014) and $2.6\sigma$-detection in $J$ band by (Faherty et al. 2014).

## 3.3 Comparison with models and discussion

We compare the ensemble of observations of WISE 0855-07 to atmospheric spectral models of cool substellar objects. We considered the full set of model spectra from Morley et al. (2014) and Burrows et al. (2003), both of which extend well below 300 K and include the effects of water clouds. Figures **??** and **??** show the observations and several selected models with $T_{eff}$ ranging from 200 to 300 K. For each model, we compute the flux expected in the Spitzer/IRAC 3.6 $\mu$m and 4.5 $\mu$m channels and scale the models to the observed Spitzer fluxes using the approach described by Rayner et al. (2009). We convert these scale factors to physical radii, which are listed in the figure legend.

None of the models match all the data, but models with $T_{eff} \lesssim 250$ K give the most reasonable agreement. Most notable is that no model faithfully reproduces the observed [3.6] - [4.5] color; models hotter than 300 K begin to match this color, but predict optical/NIR fluxes that would have been easily detected. Moreover, the physical radii of 0.5 and 0.6 $R_{Jup}$ required to fit 300 K Morley et al. and 280 K Burrows et al. models, respectively, are smaller than radii predicted from equations of state of very low-mass objects. A larger coverage fraction of cold clouds for models of $T_{eff} = 300$ K would give more reasonable radii, but disagrees with the upper limits. The Burrows et al. models show a significant discrepancy with the Morley et al. models at $\lambda < 1.2\,\mu$m. The best-fitting Morley et al. 250 K models and cooler, heavily-clouded ($h \gtrsim 0.8$ in the nomenclature of Marley et al. 2010; Morley et al. 2014) models predict $z$-band fluxes above our detection limit, so our observations nominally exclude these models. Although atmospheric models with $T_{eff} = 200$ K and a partly-cloudy atmosphere ($h = 0.5$) agree with most published upper limits, they formally disagree with the upper limit of W4 < 9 mag reported by Luhman (2014). Models below ≈200 K have [4.5] – [W4] colors that are excluded by existing data. The coolest models plotted in Figures 2 and 3 predict radii of 1.4 $R_{Jup}$; this value is larger than predicted by evolutionary models, but would be consistent with an unresolved, near-equal-mass binary. A similar situation holds with the models of Burrows et al. (2003), shown in Fig. 3, where the hotter models are too bright in the NIR and the cooler models are too bright at W4. Thus, every model disagrees with the 3.6 $\mu$m point and at least one other bandpass. The methane molecular band is the most significant opacity source at 3.6–4.5 $\mu$m, therefore the inconsistency

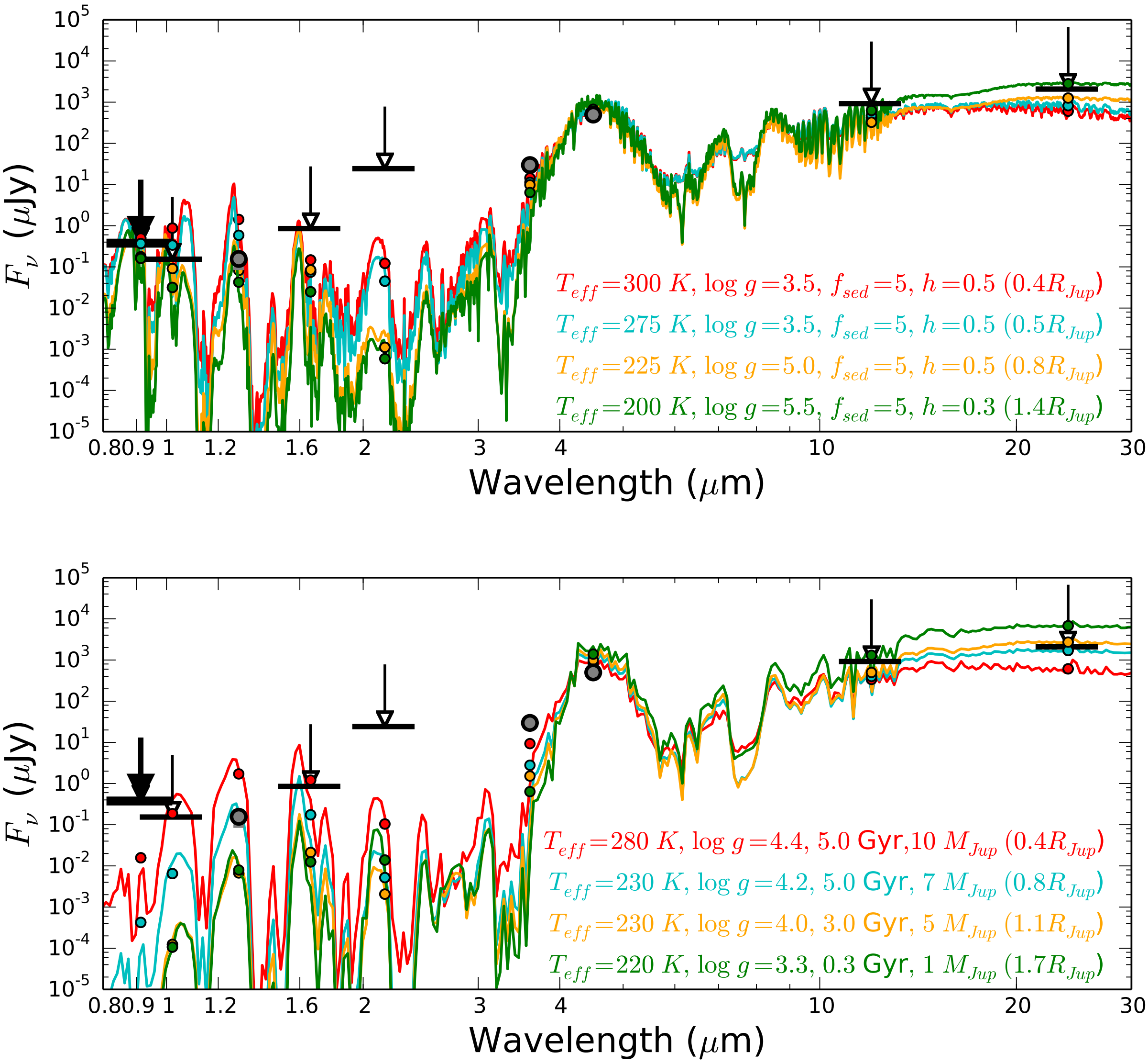

Figure 3.2: Morley et al. (2014) (top) and Burrows et al. (2003) (bottom) atmospheric models for various effective temperatures $T_{eff}$, surface gravities $\log g$, and cloud sedimentation parameters $f_{sed}$. Large grey filled circles are detections using WISE (Wright et al. 2010) and Spitzer, and the $2.6\sigma$ $J$-band detection by Faherty et al. (2014). Large arrows are upper brightness limits from Luhman (2014), Wright et al. (2014) and Beamín et al. (2014). The small color-coded dots are fluxes in photometric bands predicted by the models. Our upper limit is highlighted at far left. All photometric measurements are on the AB system. The hottest model shown is ruled out both by the upper limits and by the physically implausible radius required to match the detections.

between theoretical predictions and observations at this wavelength range might be explained by missing and/or incorrect line opacities. Alternatively, the mismatch between observations and models could indicate a more shallow temperature-pressure profile than predicted by current theory or by non-equilibrium chemistry (e.g. vertical mixing) as suggested for some directly imaged giant exoplanets (e.g. Skemer et al. 2014).

Based on the evolutionary models of Saumon & Marley (2008), at an age of 10 Gyr a 200 K object must have a mass $\leq 15\ M_{Jup}$ and radius $\approx 1.0\ R_{Jup}$. These constraints suggest that WISE 0855-07 should have $\log g \lesssim 4.5$; the plotted model spectrum with the faintest optical/NIR fluxes corresponds to $\log g = 5.0$, which would be formally excluded based on evolutionary considerations. Nonetheless even this model predicts a $z$-band flux only ~4× fainter than our limit, and the model with 200 K and $\log g$=4 yields a $z$-band flux barely fainter than our new constraint; thus dedicated ground-based observations still have a role to play. Our primary conclusions are therefore that (a) based on the current state-of-the-art models, WISE0855-07 has $T_{eff} \lesssim 250$ K and (if patchy) $\lesssim$80% of the surface is cloud-covered, and (b) improvements in models of substellar evolution, atmospheres, clouds, and opacities will be necessary to better characterize this object. WISE 0855-07 has the potential to become the first object outside the Solar system with detected water clouds in its atmosphere.

Several other groups have published follow-up studies of WISE 0855-07. Luhman & Esplin (2016), Schneider et al. (2016), and Zapatero Osorio et al. (2016) published the near-infrared photometry for WISE 0855-07 using ground-based and space observations. All three groups of authors report that several observed colors of WISE 0855-07 disagree with model predictions. The authors suggest that it might be due to either missing/incorrect methane opacities, or incomplete treatment of water cloud, or disequilibrium chemistry effects, or the combination of all the listed factors.

Skemer et al. (2016) obtained the first mid-infrared spectra for the object and compared it with model predictions and spectra of Jupiter. The authors showed that even though the spectrum of WISE 0855-07 mostly resembles that of Jupiter (e.g. dominated by water absorption), it does not show the strong $PH_3$ absorption seen in Jupiter. This likely implies that WISE 0855-07 has less turbulent mixing than Jupiter.

The most recent studies on WISE 0855-07 enable us to conclude that our theoretical understanding of atmospheres at such low temperatures is still incomplete. Further observations of WISE 0855-07 and similar objects will allow us to better constrain atmospheric models and to bridge the gap between brown dwarfs and giant exoplanets.

# Chapter 4

# Characterization of the AB Pic system

## 4.1 Introduction

Giant exoplanets and brown dwarfs around stars occur at the latest stage of star formation when a star hosts a circumstellar disk containing dust particles and gas. Nowadays, several hypotheses of formation of substellar companions and giant exoplanets exist. One of them, the core accretion (CA) scenario, suggests that a protoplanetary rocky core grows until it reaches a critical mass ($\sim$ 10 $M_{Earth}$), where accretion onto the core can start. The gas-only runaway accretion is expected to occur within 40–50 AU from a star (Pollack et al. 1996; Rafikov 2011), whereas mixed gas-solid or solid-only (pebble) accretion is possible at larger separations (up to several tens of AU; Lambrechts & Johansen 2012). The planet population synthesis by Mordasini et al. (2009) has demonstrated that CA can easily form companions with masses up to 20 $M_{Jup}$ and that formation of more massive objects by CA is unlikely. The other mechanism proposes that brown dwarf and exoplanets can fracture directly from the circumstellar disk through gravitational instability (GI; Boss 1997; Stamatellos & Whitworth 2009). Companions formed by GI are predicted to appear at separations $>$ 20 AU and exceed the mass of 13 $M_{Jup}$ (Forgan & Rice 2013). Therefore, companions formed by GI are believed to have higher mass and appear at larger separations, whereas exoplanets formed by CA have lower predicted mass and form closer-in. However, there is a number of directly imaged companions in the mass range of 5–12 $M_{Jup}$ that appear at relatively large separations from their host stars (e.g. Marois et al. 2008; Delorme et al. 2013; Rameau et al. 2013). An outward migration mechanism (e.g. Crida et al. 2009; Kley & Nelson 2012) may explain the current architecture of such systems. On the other hand, it is suggested that the molecular cloud fragmentation, that is the main mechanism for formation of multiple stellar systems, is able to produce with companions down to 5 $M_{Jup}$ (e.g. Bate 2009; Brandt et al. 2014). Nevertheless, the uncertainty in the dynamical evolution of very low-mass companions introduces additional ambiguity to our understanding of their formation mechanisms.

Chemical analysis of atmospheres of giant exoplanets and brown dwarf companions may help to resolve the controversy introduced by possible companion migration. Three main molecular components of the protoplanetary disk - water ($H_2O$), carbon dioxide ($CO_2$) and carbon oxide (CO) - have different condensation temperature, and hence, their ”icelines” are located at different radii of the disk, which affects the amount of gaseous carbon and oxygen throughout the disk (Fig. 4.1; Öberg et al. 2011): the amount of gaseous carbon is increasing, while the amount of gaseous oxygen is decreasing outwards the disk. This leads to the increase of a C/O ratio with disk radius. Therefore, a gaseous C/O ratio in the atmosphere of a giant exoplanet or a brown dwarf may indicate a formation site of the object in the disk and its formation mechanism. Objects formed by GI or molecular cloud fragmentation are expected to have a C/O ratio resembling the one of the host star, whereas objects formed by CA may have various C/O ratio depending on where in the disk their formation occurred.

There have been several efforts to measure C/O ratios in atmospheres of hot Jupiters (e.g. Benneke 2015), brown dwarfs (Line et al. 2014, 2015), and directly imaged giant exoplanets (Konopacky et al. 2013). In the latter study, Konopacky et al. used medium resolution ($R$ = 4000) K-band spectra of the directly imaged exoplanet HR8799c in comparison with a grid of pre-calculated atmospheric models with various C/O values. They found that the best-fit model corresponds to C/O = 0.65, which is slightly higher that the solar value of 0.55. Based on this results, the authors were able to exclude the gas-only CA scenario (C/O > 0.9) and tentatively CA with a large amount of solids (C/O < 0.6) for the current location of HR8799c. Mixed gas/solid CA and GI scenarios may still persist in the formation of HR8799c.

Konopacky et al. (2013) assumed the solar composition for the planetary host, HR8799. Since HR8799 has an early spectral type (A5 to F0; Gray et al. 2003), the direct abundance measurement for this star is extremely challenging, due to the lack of lines in its spectrum. However, as it was shown by Fortney (2012), even stars in the solar neighborhood may have significant derivations of a C/O ratio from the solar value. This would affect predicted C/O values throughout a circumstellar disk, consecutively, the judgement about possible formation mechanisms for certain systems with very low-mass companions. This issue has motivated us to perform a C/O ratio study for giant exoplanets/brown dwarfs and their host in complex.

In this chapter, I perform abundance measurements in the AB Pic A+B system as a test case for this effort. AB Pic is a K1V type (Torres et al. 2006) with a planet/brown dwarf companion (13–14 $M_{Jup}$ assuming the age of 30 Myr) at 260 AU orbital separation (Chauvin et al. 2005). The architecture of the system and the companion’s mass provides us with a unique opportunity to test

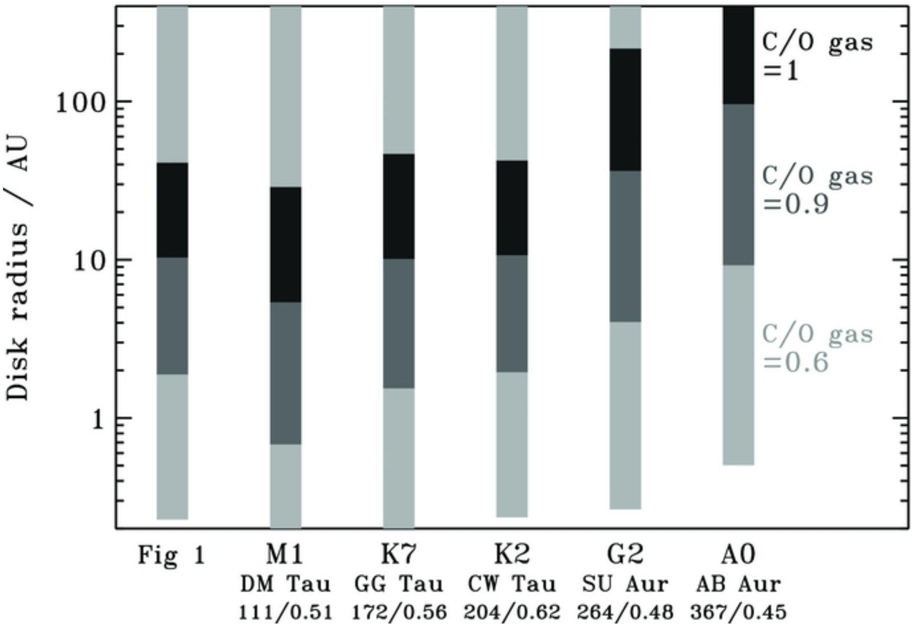

Figure 4.1: Predicted gas-phase C/O ratio as a function of radius for five representative disks, ordered by spectral type (Öberg et al. 2011).

the feasibility of measuring a C/O ratio to understand companion's formation. The companion, AB Pic B, was thoroughly analyzed by Bonnefoy et al. (2010, 2014) using medium-resolution near-infrared spectra. Bonnefoy et al. (2010) derived model-dependent parameters for AB Pic B leading to $T_{eff} = 2000^{100}_{-300}$ K, $\log g = 4.0 \pm 0.5$ dex, and SpT = L0-L1, whereas Bonnefoy et al. (2014) revised those results obtaining $T_{eff} = 1800^{100}_{-200}$ K, $\log g = 4.5 \pm 0.5$ dex, and SpT = L0 ±1. The difference in parameters between these two studies is mainly due the use of an updated version of atmospheric models in the latter study.

In the presented study, I will characterize the host star and revise the parameters for the companion. Moreover, the companion will be characterized using a novel fitting method that allows to take into account possible systematic effects that originate from models and/or observed data.

## 4.2 Characterization of AB Pic A

AB Pic was observed with Feros, La Silla between February 7 and 10 and reduced using the FEROS pipeline. Several exposures were made, and should be co-added to obtain a higher signal-to-noise ratio (SNR). However, AB Pic rotates with 12.6 km/s, has spots, and a variability period of 3.7 days. Hence, in order not to smear out spectral features using observations of different stages in the variability, we only co-add spectra from the same night. Then we select the spectra for further analysis from the night that yields the largest signal-to-noise ratio. Prior to the co-addition the spectra were radial velocity shifted and normalised.

An initial analysis of the stellar parameters was conducted using only the spectra. This resulted in a cool atmosphere that could not reproduce many of the spectral features in the spectrum synthesis. Therefore, we determined the temperature from $V - Ks$ using the de-reddening from Schlafly & Finkbeiner (2011). Using Hipparcos parallax measurements (van Leeuwen 2007) and the bolometric correction for AB Pic A, we were able to calculate surface gravity.

First equivalent widths of Fe lines were determined using IRAF by measuring Fe lines from a line list from Hansen et al. (2011, 2012), however, this list was developed for normal dwarfs and giants without strong molecular features, and this resulted in values $\sim 0.25$ dex lower than literature suggests. One of the reasons for this is that setting the continuum accurately in a star with spots and molecules can be challenging, and such features can easily introduce biases in the equivalent widths measured. Therefore, the [Fe/H] was calculated conducting a spectrum synthesis over large spectral regions around 40 carefully selected Fe lines (Bean 2007) in regions containing fewer molecular bands. This results in a set of final stellar parameters: effective temperature $T_{eff} = 5176 \pm 80$K, surface gravity $\log g = 4.50 \pm 0.05$, metallicity $[Fe/H] = -0.11 \pm 0.15$, microturbulence $\xi = 1.40 \pm 0.15$ km/s.

We used MARCS models (Gustafsson et al. 2008) for the stellar spectral analysis. For consistency with the AB Pic B using Phoenix models (Allard et al. 2013), we compared the temperature - pressure (T-P) profiles of the MARCS and Phoenix models. No differences are found between the two model atmospheres using these stellar parameters in the outer layers where the lines of interest (C, O) were formed. We thus consider it consistent to continue the analysis with MARCS[1]. In the following the 1D MARCS models together with the 1D, LTE spectrum synthesis code MOOG, version 2014 (Sneden 1973). The line list was downloaded from the Vienna Atomic Line Database, VALD (Kupka et al. 2000) and updated with information from NIST[2] and the Kurucz database[3]. The list was then calibrated on the Sun, and it can reproduce the features in the high-resolution, high SNR BASS2000[4] solar spectra.

To measure oxygen abundances using lines that have been discussed in Caffau et al. (2008, 2013), the oxygen triplet at 7771−7775 Å. For carbon abundance we use the line at 5380 Å which one of the few carbon lines reaching a flux level deeper than 3% of the normalised flux, which we require to ensure that the detection is reliable and outside the noise. Based on these lines we obtain a $[C/O] = -0.01 \pm 0.04$. The uncertainties in the line profile fitting and those propagating

---

[1] Converting the Phoenix models into MOOG format was not possible and we therefore stuck with MARCS models after this comparison.

[2] http://physics.nist.gov/PhysRefData/ASD/lines_form.html

[3] http://www.pmp.uni-hannover.de/cgi-bin/ssi/test/kurucz/sekur.html

[4] http://bass2000.obspm.fr/solar_spect.php

| Parameter | Δ[C/Fe] | Δ[O/Fe] |
|---|---|---|
| T (5176 ± 80K) | 0.04 | 0.10 |
| $\log g(4.5 \pm 0.05)$ | 0.03 | 0.02 |
| [Fe/H] (−0.1 ± 0.15) | 0.01 | 0.03 |
| $\xi(1.4 \pm 0.15\,\mathrm{km/s})$ | 0.03 | 0.01 |
| Continuum+fitting | 0.2 | 0.05 |
| Total (propagated): | 0.21 | 0.12 |

Table 4.1: Measurement uncertainties for AB Pic A.

from uncertainties in the stellar parameters are listed in Table 4.1.

### 4.2.1 The fitting method

Synthetic spectra calculated using atmospheric models may contain know (and unknown) uncertainties and systematic effects, such as missing or incorrect opacities, mistreatment of convection and disequilibrium chemistry, etc. Morever, observations themselves can have unaccounted systematic effects that were missed during data reduction. In order to take into account possible systematics when comparing observations to models, I have created a novel model fitting method.

Let's assume that we have observed spectra with $N$ flux measurements, $y_{\lambda_n}$ with corresponding uncertainties $\sigma_{y_n}$, where $n = 1 \ldots N$. The treatment of possible systematic effects starts from the following consideration of the relation between synthetic (model) $m(\lambda)$ and the observed spectra $y(\lambda)$:

$$y(\lambda_k) \approx f(\lambda_k) \cdot m(\lambda_k), \tag{4.1}$$

where $k = 1 \ldots K$ is a number of the used wavelength points and $f(\lambda)$ is the fitting vector. If $K = N$ than the fitting function is calculated for every wavelength point ob the model and observations, and the observation vector $g(\lambda)$ is identical to the sum in Eq. 4.1. However, since I try to find trends in relation between models and observations, rather than the exact fitting vector that would match them to each other, $K$ should be much smaller than $N$, in order to avoid over-fitting.

In this case, I use a trigonometric polynomial as a from for the fitting vector. I avoid using a classical polynomial because they are poorly constrained on the edges of the data segment, while trigonometric polynomials do not have this disadvantage. The trigonometric basis $H_{N,2K+1}$ for the fitting vector $f(\lambda)$ is:

$$H_{2K+1,N} = \begin{pmatrix} 1 & 1 & \cdots & 1 \\ \cos\frac{2\pi\lambda_1}{L} & \cos\frac{2\pi\cdot\lambda_2}{L} & \cdots & \cos\frac{2\pi\cdot\lambda_N}{L} \\ \cos\frac{2\cdot 2\pi\lambda_1}{L} & \cos\frac{2\cdot 2\pi\cdot\lambda_2}{L} & \cdots & \cos\frac{2\cdot 2\pi\cdot\lambda_N}{L} \\ \vdots & \vdots & \ddots & \vdots \\ \cos\frac{K\cdot 2\pi\lambda_1}{L} & \cos\frac{K\cdot 2\pi\cdot\lambda_2}{L} & \cdots & \cos\frac{K\cdot 2\pi\cdot\lambda_N}{L} \\ \sin\frac{2\pi\lambda_1}{L} & \sin\frac{2\pi\cdot\lambda_2}{L} & \cdots & \sin\frac{2\pi\cdot\lambda_N}{L} \\ \sin\frac{2\cdot 2\pi\lambda_1}{L} & \sin\frac{2\cdot 2\pi\cdot\lambda_2}{L} & \cdots & \sin\frac{2\cdot 2\pi\cdot\lambda_N}{L} \\ \vdots & \vdots & \ddots & \vdots \\ \sin\frac{K\cdot 2\pi\lambda_1}{L} & \sin\frac{K\cdot 2\pi\cdot\lambda_2}{L} & \cdots & \sin\frac{K\cdot 2\pi\cdot\lambda_N}{L} \end{pmatrix} \tag{4.2}$$

where $L$ is the scaling factor and should take a value of the order of the studied wavelength range.

Let me introduce the matrix $A_{N,2K+1}$:

$$A_{2K+1,N} = H_{2K+1,N} \times \begin{pmatrix} f(\lambda_{11}) & 0 & \cdots & 0 \\ 0 & f(\lambda_{22}) & \cdots & 0 \\ \vdots & \vdots & \ddots & \vdots \\ 0 & \cdots & \cdots & f(\lambda_n) \end{pmatrix} \tag{4.3}$$

Therefore, the introduced problem can be described in the follwoing matrix equation where X is the vector of coefficients for the trigonometric polynomial.

$$Y_N = A_{N,2K+1} X_{2K+1} \tag{4.4}$$

Since for the purposes of the problem, $K$ should be much less than $N$ (because I aim to determine a trend rather than funding an exact fit), the matrix equation above cannot have an exact solution. However, I can re-establish the problem in the following way:

$$X_{2K+1,1} = \begin{pmatrix} k_1 \\ k_2 \\ \cdots \\ k_{2K+1} \end{pmatrix} = (A^\top C^{-1} A)^{-1} (A^\top C^{-1} Y), \tag{4.5}$$

which allows me to weight spectral fluxes with uncertainties and reduce the dimensiality.

Fig. 4.2 shows fitting vectors for models with different set of physical parameters. As can be seen, each model has its individual fitting vector. I needed to select a model with which an optimal fitting vector could be calculated. For that I can marginalized over all the fitting vectors leading to the following $\chi^2$ value:

$$\chi^2 = y^\top V^{-1} y \tag{4.6}$$

Where $V = C + A\Lambda A^\top$ By minimazing the $\chi^2$ value, I was able to determine an optimal model to calculate the fitting vector.

### 4.2.2 Results

To apply my method, I use BTSettl atmospheric models (Allard et al. 2013). The BTSettl models take into account dust gravitational settling at temperatures $T_{eff} \approx 2700$K following the approach described in Rossow (1978). Radiative transfer calculations are performed using PHOENIX atmosphere code (Allard et al. 2001). Atomic and molecular opacities are treated line-by-line using the list of Allard et al. (2003). Non-equilibrium chemistry effects for $CH_4$, CO, $CO_2$, $N_2$, and $NH_3$ are treated using height-dependent diffusion based on radiation-hydrodynamic simulation of (Freytag et al. 2010). The reference solar abundance are based on CIFIST photospheric abundance from Caffau et al. (2011).

I performed separate analysis for $J$, $H$, and $K$ bands separately. The optimal model to calculate the fitting vector for $J$ band has parameters of $T_{eff}$=1600K, $\log g$=5.5, [Fe/H]=0.0, and [C/O]=0.0; for $H$ band - $T_{eff}$=1700K, $\log g$=4.5, [Fe/H]=0.0, and [C/O]=+0.2; and finally, for $K$ band - $T_{eff}$=1600K, $\log g$=3.5, [Fe/H]=0.0, and [C/O]=+0.2. I have calculated the fitting vector separately for each band, using their individual optimal models.

After applying fitting vectors for all the models using Eq. 4.1, I performed the least-square minimization when comparing the adjusted models to observed spectra. The best-fit parameters are the following: for $J$ band - $T_{eff}$=1600K, $\log g$=5.00 dex, [Fe/H]=0.0, and [C/O]=0.0; for $H$ band - $T_{eff}$=1700K, $\log g$=4.5, [Fe/H]=0.0, and [C/O]=+0.2; and finally, for $K$ band - $T_{eff}$=1600K, $\log g$=3.5, [Fe/H]=0.0, and [C/O]=+0.2.

Additionally, I ran a classical least-square fit minimization comparing models to observations without applying any adjustments. I have obtained the following parameters: for $J$ band is $T_{eff}$=1600K, $\log g$=3.5, [Fe/H]=0.0, and [C/O]=-0.3; for $H$ band - $T_{eff}$=1400K, $\log g$=4.0, [Fe/H]=0.0, and [C/O]=+0.2; and finally, for *K* band - $T_{eff}$=1800K, $\log g$=4.0 , [Fe/H]=0.0, and [C/O]=+0.2.

The results are summarized in Table 4.2 and discussed in the next section.

| Parameter | *J* band | | *H* band | | *K* band | |
|---|---|---|---|---|---|---|
| | Original | Adjusted | Original | Adjusted | Original | Adjusted |
| $T_{eff}$, K | 1600 | 1600 | 1400 | 1700 | 1800 | 1700 |
| $\log g$ | 3.5 | 5.0 | 4.0 | 4.5 | 4.0 | 3.5 |
| [Fe/H] | 0.0 | 0.0 | 0.0 | 0.0 | 0.0 | 0.0 |
| [C/O] | -0.3 | 0.0 | +0.2 | +0.2 | +0.2 | +0.2 |

Table 4.2: The results of model fitting with and without applying of the fitting vector.

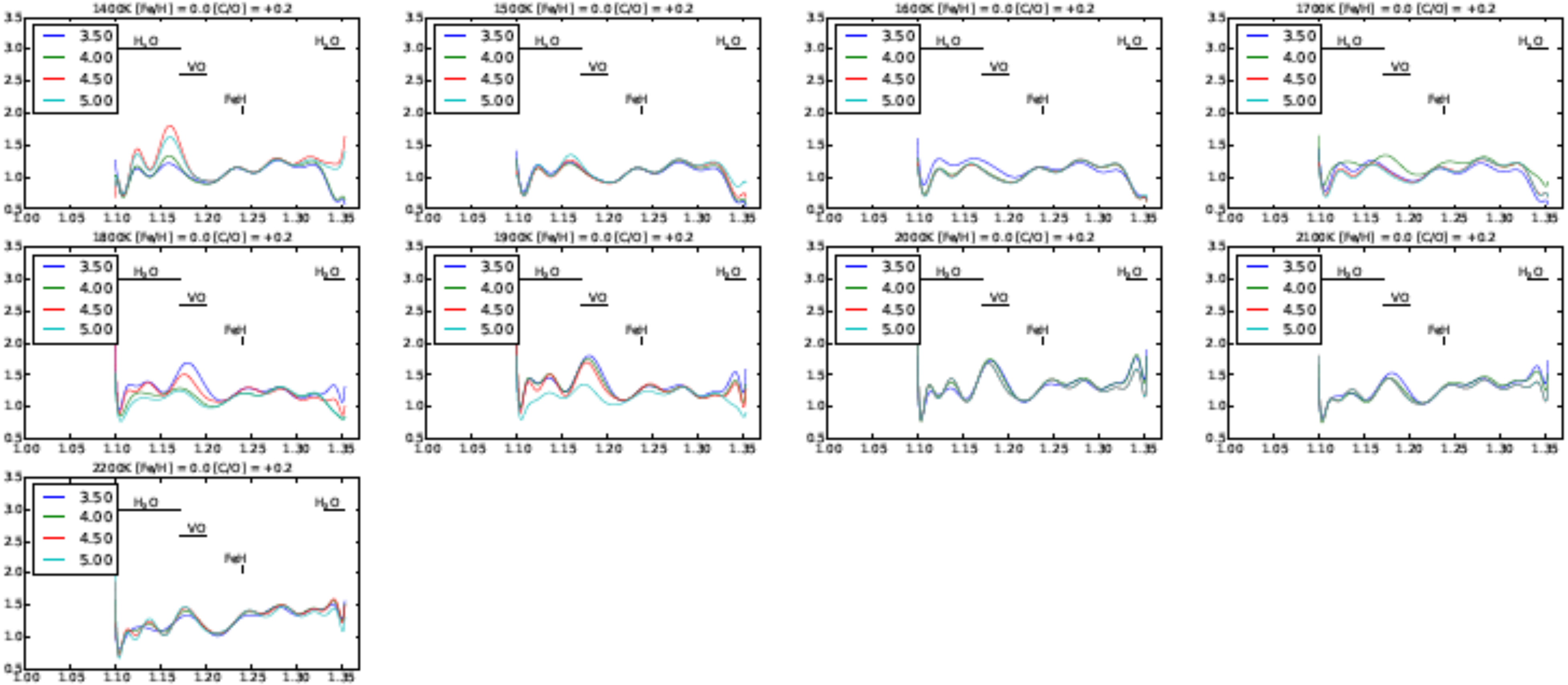

Figure 4.2: Fitting vectors for various models with [C/O]=+0.2. The fitting vectors are over-plotted with the position of various molecular bands at certain wavelengths. The bar on the top left corner indicates values of log $g$.

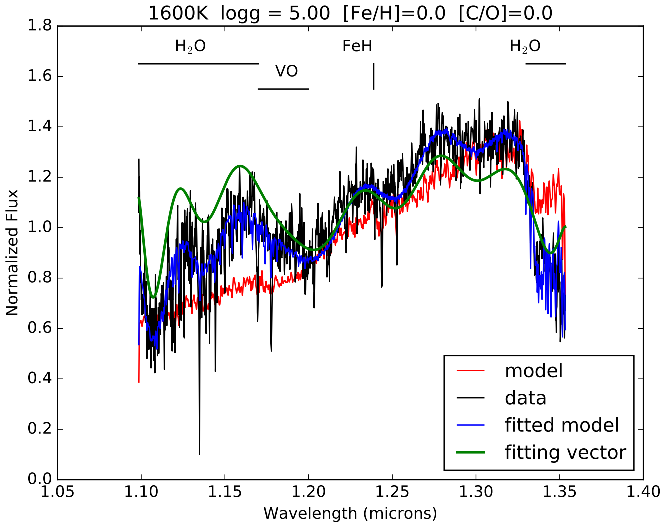

(a) *J* band

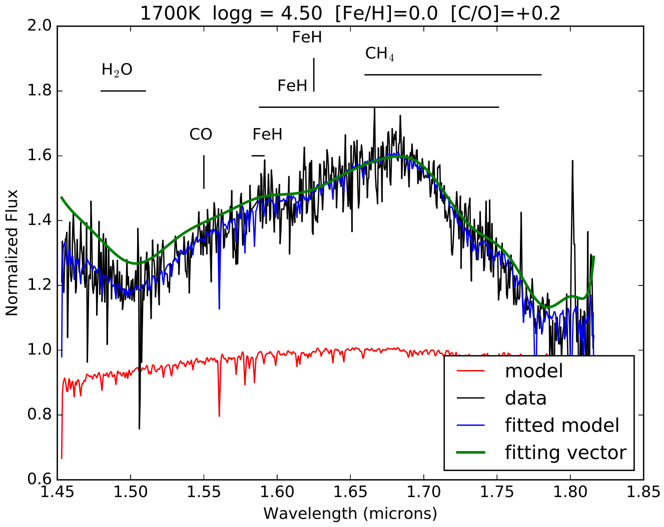

(b) *H* band

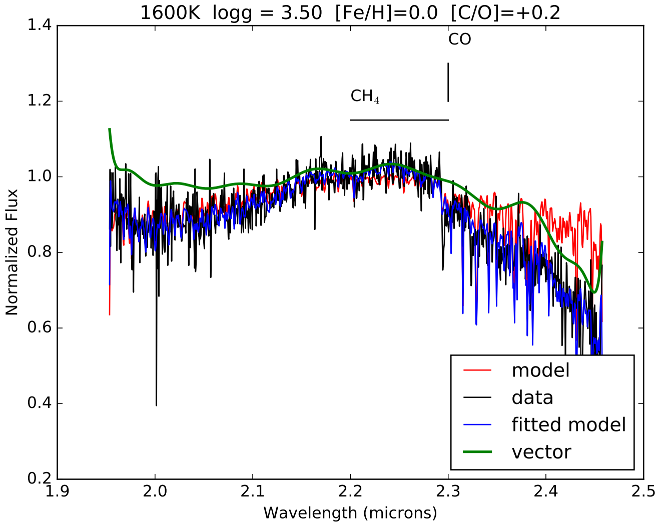

(c) *K* band

Figure 4.3: The results of the described fitting method. Black lines are observed spectra, red lines are original models, green lines are fitting vectors, and blue lines are adjusted models.

## 4.3 Discussion

In this chapter, I aimed to study the AB Pic study, characterizing both the host star and the companion. To characterize the host star, I applied classical methods using tools available through MOOG. The important outcome of this characterization is that I measured solar-like metallicity and a C/O ratio for AB Pic A. This results strongly simplifies (or rather does not complicate) the further analysis for AB Pic B.

To characterize the companion, AB Pic B, I have developed a novel method that allows to take into account systematic effects induced by models and/or observations and data treatment. Effective temperature has a value of 1600–1800 K and is consistent with the results of Bonnefoy et al. (2014). On the other hand, surface gravity cannot be constrained precisely and may take values in the range of $\log g = 3.5 - 5.0$. Interestingly, that using both original and adjusted models, I could derive solar values for metallicity in AB Pic B. It is expected that metal-rich disk will more effectively form giant exoplanets by core accretion, however, there is no evidence that this process cannot occur in disks with solar metallicity. On the other hand, the measured C/O ratio of [C/O]=+0.2 gives preference to the scenario where AB Pic B was formed by core accretion at 10-50 AU (see Fig. 4.1) and then scattered or migrated to a more distant orbit. The non-solar C/O ratio allows us to exclude a binary-like formation scenario for the AB Pic system. Additionally, if we assume that a companion formed by gravitational instability will use mixed material from the disk, the non-stellar C/O ratio allows us to exclude this formation scenario for AB Pic B as well.

Another uncertainty is introduced by our capability to measure abundances with a good precision. Even though, I have demonstrated that various systematic effects do not affect effective temperature much, the other parameters are under bigger danger. The brightest example for that statement is best-fits parameters obtained using the region of *J* band (Table 4.2). The least square minimization using the original models provided us with [C/O]=-0.3 which is strongly inconsistent with the results obtained using the other wavelength regions. A careful look at Fig. 4.3 allows us to notice that the systematic vector shows the strongest effect at the wavelength region where one of the water bands appears. A similar behavior of the systematic vector can be seen in *H* band spectra. Indeed, when the systematic vector is applied, the least-square minimization using the adjusted models allow us to get different C/O ratios that are more consistent with the results obtained at the other wavelength regions.

Even though, I can speculate that this inconsistency is introduced by the water band, I cannot be sure if it originates in models or observations. It can be either missing/incorrect opacities uses to calculate spectra in BTSettl models, or, for instance, an inaccurate telluric correction was applied to account for water absorption in the Earth's atmosphere during observations. I can disentangle these two possibilities by applying the described method using several models that implement different opacity lists. Hence, the method can also be used as a powerful tool to pick a better model for characterization of an object of interest.

Summarizing, the obtained result has demonstrated that the precision of abundance measurements may not be high enough yet to use it for understanding formation. Various systematic effects are still an obstacle to robust abundance measurements. Moreover, even if one can get very precise estimates for abundances, various processes, such as companion migration, may complicate the picture. Therefore, even though abundances-based studies of formation are promising, they need to be interpreted with caution.

# Chapter 5

# Summary and Discussion

In this dissertation I presented several studies that concentrated on the characterization of atmospheres of directly imaged (sub-)stellar objects, as well as in defining a benchmark sample to test atmosphere and interior models.

In one of the presented studies (Chapter 3; Kopytova et al. 2016) I presented the "single-star" sequence in the Hyades open cluster. In total, we identified 250 members of the cluster that do not show signatures of a companion outside the 2–7 AU projected separation (depending on the distance to each individual member and the survey, see Appendix A for the table with a full list of the 250 stars). Comparison of the near-infrared properties of the single-star sequence with theoretical isochrones shows an overall good agreement for the mass range 0.13–2.30 $M_\odot$. The only disagreement between models and observations is that for masses below 0.6 $M_\odot$ the observed $J - Ks$ and $H - Ks$ colors are systematically redder than the isochrones by 0.05 mag. I showed that open clusters can be a powerful tool for testing interior and atmospheric models. I also mentioned the study of Douglas et al. (2016) where the authors used the benchmark sequence to exclude possible binary and multiple systems when studying rotational periods in the Hyades to test the existing gyrochronological relations.

The other presented study (Chapter 2; Kopytova et al. 2014) attempted to characterize the coolest know Y dwarf, WISE J085510.83-071442.5, in particular, to constrain the presence of water ice clouds in its atmosphere. I concluded that: (a) WISE0855-07 has Teff of 200–250K, (b) < 80% of its surface is covered by clouds. Moreover, I cited several follow-up papers that pursued to further characterize WISE0855-07, either by using photometry (Luhman & Esplin 2016; Schneider et al. 2016; Zapatero Osorio et al. 2016), or spectroscopy (Skemer et al. 2016). The ensemble of these studies has shown that

Chapter 4 was dedicated to studying parameters of AB Pic system. I attempted to characterize the host star and its companion in ensemble. I have created a method that allows to take into account various systematic effects introduced by observations and models. I have demonstrated how fixing these effects may influence final results.

## 5.1 Open questions and future prospects

### 5.1.1 Inaccuracies in models or peculiar data?

In Chapter 3 it has been shown that none of the two recent generation atmospheric models that include effects of water ice clouds in brown dwarfs (Burrows et al. 2003; Morley et al. 2014) can reproduce the observed spectral energy distribution (SED) of the object of interest, the coolest known Y dwarf WISE J085510.83-071442.5 (WISE 0855-07; Kopytova et al. 2014). The mismatch between models and observations is particularly prominent at the wavelength range 3.6–4.5 $\mu$m, where the methane molecular band is predicted to be the most significant opacity source. Thus, the inconsistency between modeled and observed SEDs can be explained by incorrect/missing line opacities used to calculate synthetic photometry. Alternatively, the mismatch between models and observations could be explained by a more shallow temperature-pressure profile than predicted by current theory. On the other hand, this mismatch could also indicate the presence of non-equilibrium chemistry effects in the atmosphere of WISE 0855-07. It would cause the atmospheric vertical mixing leading to an excess of carbon oxide and the deficiency of methane. The non-equilibrium chemistry effect influencing the appearance of the methane absorption around 3.3 $\mu$m was previously reported for directly imaged giant exoplanets 2M1207b and HR8799bcde by Skemer et al. (2014).

The described study has shown the need to test models, in order to understand the origin of the inconstancy between theoretical predictions and observations - whether it is caused by incorrect models or certain peculiarities in observed objects. In Chapter 2 I described my paper defining the single-star sequence in the Hyades to use it as a benchmark for testing theoretical predictions (Kopytova et al. 2016). I have shown that new-generation theoretical isochrones describe the observed sequence well. In particular, the improvement in comparison with older-generation models can be noticed at the “knee-shaped” part of the isochrones around 0.4–0.8 M$\odot$, which is most plausibly due to the upgraded treatment of the equation of state. However, it can be seen that the observed sequence is systematically redder than the theoretical isochrones by $\sim$ 0.05 mag at masses lower than 0.6 M$\odot$ on $J - K_s$ and $H - K_s$ diagrams. This can be due to missing or incorrect opacities in the used atmospheric models.

Even though benchmark systems, such as open clusters, are excellent tools to detect problems with theoretical models, they cannot identify what these problems are particularly. Even though a mismatch between theoretical and observed isochrones may suggest that there are some opacities missing, it cannot give a hint which particular atomic or molecular bands (i.e. which wavelength) should be revised. Moreover, quite often no benchmarks are available before a model will be applied for characterization of an isolated object. These two issues motivated me to develop a novel method that allows to test models on the fly simultaneously identifying problematic wavelength regions, as described in Chapter 4. The "fitting vector" enable us to determine and diagnose for potential systematic effects in models and data. In the further development, it will be possible to determine another vector that would also describe the dependence of systematic based not only on the wavelength region but also on a region in the parameter space (see Section 5.1.2).

### 5.1.2 Future of techniques for characterization sub-stellar objects

As mentioned before, traditionally, atmospheres of exoplanets and brown dwarfs are studied by the comparison observations to a grid of model simulated spectra. The grid-based comparison approach has a strong advantage of being physically self-consistent. Typically, these models calculate the pressure-temperature profile and chemical abundances in the atmosphere until a solution converges. However, most of these models exist under several assumptions, such as thermochemical equilibrium, or solar-like abundances. Furthermore, grid-based models come without uncertainties for included physical and chemical processes.

On the other hand, the retrieval approach inverts observed spectra into constraints on physical parameters. In comparison to forward modeling, the retrieval approach does not aim to self-consistently simulate physical or chemical processes in the atmosphere. Instead, the atmospheric structure is directly parametrized with variables to produce a spectrum to directly compare it to observations. Typically, the parametrized variables include temperature profile, surface gravity, radius, and chemical abundances. At the end, parameters are retrieved through multiple calculations of synthetic spectra using the parametrized model. The big advantage of the retrieval approach is that it is able to produce uncertainties based on priors and the response of the parametrized model to a change in parameters (i.e. how flux at each wavelength changes with varying parameters). The outcome of the retrieval approach is a posterior distribution over parameters. Recently, the retrieval approach has been actively exploited in studies of exoplanet and brown dwarf atmospheres (e.g. Line et al. 2014, 2015; Benneke 2015). However, the retrieval approach has certain disadvantages. The main disadvantage is the over-simplified description of chemical and physical parameters in the atmosphere. These issues can be addressed in future studies.

The physical over-simplification of the retrieval approach may produce unrealistic atmospheric parameters. Basically, the retrieval approach allows data to derive the final solution even if it is unphysical. It is essential to develop a merit that would allow us to quantify the physical plausibility of the results from the retrieval approach. As an future scientific opportunity, I plan to apply the method described in Chapter 4 to study how synthetic spectra calculated using various self-consistent models change with varying parameters. This will allow us to diagnose spectral features that are sensitive to changes of certain parameters and to calibrate the parametrized model.

Machine learning has been used before for stellar classification and parameter determination. Bailer-Jones et al. (1997) used artificial neural networks to derive effective temperature and metallicity for 5000 spectra of stars ranging B2–M7 spectral types. This study continued with the neural network implementation for spectral classification in Bailer-Jones et al. (1998). Most recently, Ness et al. (2015) used a generative model calculated from a training set of 542 stars to derive parameters ($T_{eff}$, $\log g$, [Fe/H]) for 55,000 stars. With growing observational capabilities, it is becoming possible to apply machine learning techniques to observations of brown dwarfs and directly imaged giant exoplanets. Nowadays, there are several brown-dwarf/giant-exoplanet databases (e.g., SpeX, BDNYC) containing several hundreds of spectral templates that can be used as a training set in the machine learning process. If machine learning applied, it will open new opportunities to understand how observed fluxes (spectra and photometry) change with physical parameters in brown dwarfs and exoplanets. This may become a new way of understanding and interpreting observations when comparing them with models.

## 5.2 Conclusions

The systematic understanding of stellar atmospheres started in the 19th century with development of the very first spectral classification scheme. In the 1960s theory predicted the existence of brown dwarfs, objects so cool that they cannot sustainably burn hydrogen-1 as main-sequence stars. With growing observing capabilities in the 1990s, the detection of brown dwarfs became possible, as well as the discovery of the first exoplanet. In the new century, the scientists have successfully imaged giant exoplanets directly and detected many more planets using the transit method. All these studies made clear that atmospheres of stars, brown dwarfs, and exoplanets can be studied in ensemble - that lower-mass main-sequence stars are similar to most massive brown dwarfs, and that the coolest brown dwarfs are hard to disentangle from directly imaged giant exoplanets. New-generation ground-based instruments, such as SPHERE and GPI, as well as future 40m-class telescopes and space missions will allow us to study atmospheres of stellar and sub-stellar objects with unprecedented detail and might enable us to extend the studies beyond studies of giant exoplanets to terrestrial exoplanets (super-Earths), filling out and bridging the gap between different types of objects.

# Acknowledgements

Thank you, Richard and Tobias, for printing it out!

First of all, I would like to thank my advisor, Wolfgang Brandner, who was always guiding and supporting me. Even though, Wolfgang is not officially eligible to get credit for his fantastic supervising, this dissertation and all the papers I wrote and co-authored would not be possible without him. Wolfgang's door was always open, no matter how busy he was. He never pressured me and always supported my ideas and provided them with excellent hints and useful advice. Wolfgang fostered me as an independent researcher allowing to chaise my scientific intuition. I hope we will continue collaborating with Wolfgang.

Lisa Kaltenegger, who co-advised part of my research, was a constant inspiration and a role-model. Her passion and support always supported me encouraging to aim higher and higher. She always assured that I was a real scientist.

This research would not be possible without my collaborators Beth Biller, Mickaël Bonnefoy, Josh Schlieder, Niall Deacon, Ian Crossfield, and Esther Buenzli. Our weekly "high-contrast" coffees on Wednesdays were the favorite part of the week for me. I have learned so much from you, guys, and was getting a constant inspiration to do research. I was very lucky to have an opportunity to collaborate with you. I hope we are going to write more interesting papers together.

I want to thank Pier Giorgio Prada Moroni, Emanuele Tognelli, Sigmund Siegfried, and Elena Schilbach. I am very grateful for their help with our paper and for their patience while I was producing science.

I would also like to give all the possible credit to Emer Brady who has corrected my English in this thesis (despite the fact I used the American spelling). Emer was also among first people I met in Heidelberg and she happened to be a good and supporting friend. Her parents also own a beautiful dog and two cats, and I was privileged to visit her family (and the pets) in Ireland. So obviously, Emer is one of my favorite people.

Other amazing friends that I met in Heidelberg cannot be left out. Michael Maseda, Paolo Bianchini, Sasa Tsatsi, Ilya Khrykin, Alina Pavlova, and Miguel Querejeta. Seriously, guys, I don't know how you handled me because I'm obviously crazy. I guess you're just crazy, too. Anyway, Heidelberg was worth coming just to meet you. In the related note, anyone who was ever a resident or a regular in Office 217 should be mentioned. You are my people. In this note, Sven Buder should be mentioned separately because: a) he's a lot of fun and b) he translated the abstract of my thesis to German.

Now, the real adults should be thanked. Melissa Ness, Remco van den Bosch, Casey Deen, and Anna Sipel, somehow you decided that I was cool and I still don't know why. But I'm happy we're friends. You're amazing and you rock. Also, Matt Mechtley, Morgan Fouesneau, Carl Ferkinhoff, Mark Norris, Iskren Georgiev, and Nikolay Kacharov, you're absolutely awesome, let's quiz!! Thank you, Glenn! Thank you so much!

I want to mention Nadezhda Vlasova who helped to figure my stuff out. I'm sending a lot of love to my friend Anna Punanova who's also an astronomer and who is going to defend at some point, too. You're a wonderful friend, Anya. Even though we don't see each other often, I know that you're always there for me. My flatmate and friend Olga Kiseleva knows how I am in the routine life and she still talks to me. So she's kind of a hero. And it's amazing how crazily fun we can be together. Olya, thank you for being able to live next to me for over 5 years! Sergey Nikolaev, you already have a PhD, so you understand what I've passed through. But the sessions of crazy laugh we always have helped so much!

The New York crew: Kelle Cruz, Emily Rice, Rebecca Oppenheimer, and David Hogg. You showed me that I can do great science in my favorite city. Thank you for that. Special thanks to Ruth Angus and Dan Foreman-Mackey, not only because they're great astronomers but simply because they're cool and very nice people. And also naturally hipster.

And of course, this work would not be possible without my family. Without my dad who's an engineer and also crazy. I know where I got my brain from. Without my mom I wouldn't be able to achieve most of the things in my life. She's always there for me no matter what. She always believes in me and I got her emotional heart and romantic soul. Also, thanks to my brother, Konstantin, because he's also crazy and have the same sense of humor with me. And he also loves wine as much as I do. His son and my nephew, Vsevolod, is the one for whom I want to be adult and responsible.

And the city of Heidelberg, you are beautiful and became my home. Thank you for this.

I apologize for everyone who read all this text hoping to find their name and didn't see it. I'm terrible but I'm just incapable to remember all the people that did something important for me because there were so many of them. And this is fantastic.

# Bibliography

Ackerman, A. S., & Marley, M. S. 2001, ApJ, 556, 872

Allard, F., Hauschildt, P. H., Alexander, D. R., Tamanai, A., & Schweitzer, A. 2001, ApJ, 556, 357

Allard, F., Homeier, D., & Freytag, B. 2013, Mem. Soc. Astron. Italiana, 84, 1053

Allard, N. F., Allard, F., Hauschildt, P. H., Kielkopf, J. F., & Machin, L. 2003, A&A, 411, L473

Apai, D., Radigan, J., Buenzli, E., Burrows, A., Reid, I. N., & Jayawardhana, R. 2013, ApJ, 768, 121

Apai, D., et al. 2016, ArXiv e-prints

Appenzeller, I., et al. 1998, The Messenger, 94, 1

Asplund, M., Grevesse, N., Sauval, A. J., & Scott, P. 2009, ARA&A, 47, 481

Bailer-Jones, C. A. L., Irwin, M., Gilmore, G., & von Hippel, T. 1997, MNRAS, 292, 157

Bailer-Jones, C. A. L., Irwin, M., & von Hippel, T. 1998, MNRAS, 298, 361

Baraffe, I., Chabrier, G., Allard, F., & Hauschildt, P. H. 1998, A&A, 337, 403

Baraffe, I., Homeier, D., Allard, F., & Chabrier, G. 2015, A&A, 577, A42

Barnes, S. A. 2003, ApJ, 586, L145

Bate, M. R. 2009, MNRAS, 392, 590

Beamín, J. C., et al. 2014, ArXiv e-prints

Bean, J. L. 2007, PhD thesis, The University of Texas at Austin

Bell, C. P. M., Naylor, T., Mayne, N. J., Jeffries, R. D., & Littlefair, S. P. 2012, MNRAS, 424, 3178

Benneke, B. 2015, ArXiv e-prints

Biller, B. A., et al. 2013, ApJ, 778, L10

—. 2015, ApJ, 813, L23

Bonnefoy, M., Chauvin, G., Lagrange, A.-M., Rojo, P., Allard, F., Pinte, C., Dumas, C., & Homeier, D. 2014, VizieR Online Data Catalog, 356, 20127

Bonnefoy, M., Chauvin, G., Rojo, P., Allard, F., Lagrange, A.-M., Homeier, D., Dumas, C., & Beuzit, J.-L. 2010, A&A, 512, A52

Boss, A. P. 1997, Science, 276, 1836

Brandt, T. D., et al. 2014, ApJ, 794, 159

Buenzli, E., Apai, D., Radigan, J., Reid, I. N., & Flateau, D. 2014, ApJ, 782, 77

Buenzli, E., Saumon, D., Marley, M. S., Apai, D., Radigan, J., Bedin, L. R., Reid, I. N., & Morley, C. V. 2015, ApJ, 798, 127

Burrows, A., & Sharp, C. M. 1999, ApJ, 512, 843

Burrows, A., Sudarsky, D., & Hubeny, I. 2006, ApJ, 640, 1063

Burrows, A., Sudarsky, D., & Lunine, J. I. 2003, ApJ, 596, 587

Burrows, A., et al. 1997, ApJ, 491, 856

Caffau, E., Ludwig, H.-G., Malherbe, J.-M., Bonifacio, P., Steffen, M., & Monaco, L. 2013, A&A, 554, A126

Caffau, E., Ludwig, H.-G., Steffen, M., Ayres, T. R., Bonifacio, P., Cayrel, R., Freytag, B., & Plez, B. 2008, A&A, 488, 1031

Caffau, E., Ludwig, H.-G., Steffen, M., Freytag, B., & Bonifacio, P. 2011, Sol. Phys., 268, 255

Carney, B. W. 1982, AJ, 87, 1527

Casagrande, L. 2007, in Astronomical Society of the Pacific Conference Series, Vol. 374, From Stars to Galaxies: Building the Pieces to Build Up the Universe, ed. A. Vallenari, R. Tantalo, L. Portinari, & A. Moretti, 71

Castellani, V., Degl'Innocenti, S., & Prada Moroni, P. G. 2001, MNRAS, 320, 66

Chaboyer, B., & Kim, Y.-C. 1995, ApJ, 454, 767

Chauvin, G., et al. 2005, A&A, 438, L29

Crida, A., Masset, F., & Morbidelli, A. 2009, ApJ, 705, L148

Cridland, A. J., Pudritz, R. E., & Alessi, M. 2016, ArXiv e-prints

Crossfield, I. J. M., et al. 2014, Nature, 505, 654

Cushing, M. C., et al. 2008, ApJ, 678, 1372

—. 2011, ApJ, 743, 50

Da Rio, N., & Robberto, M. 2012, AJ, 144, 176

Degl'Innocenti, S., Prada Moroni, P. G., Marconi, M., & Ruoppo, A. 2008, Ap&SS, 316, 25

Dell'Omodarme, M., Valle, G., Degl'Innocenti, S., & Prada Moroni, P. G. 2012, A&A, 540, A26

Delorme, P., et al. 2013, A&A, 553, L5

Dotter, A., Chaboyer, B., Jevremović, D., Kostov, V., Baron, E., & Ferguson, J. W. 2008, ApJS, 178, 89

Douglas, S. T., Agüeros, M. A., Covey, K. R., Cargile, P. A., Barclay, T., Cody, A., Howell, S. B., & Kopytova, T. 2016, ApJ, 822, 47

Duchêne, G., Bouvier, J., Moraux, E., Bouy, H., Konopacky, Q., & Ghez, A. M. 2013, A&A, 555, A137

Dupuy, T. J., & Kraus, A. L. 2013, Science, 341, 1492

Dupuy, T. J., & Liu, M. C. 2012, ApJS, 201, 19

Faherty, J. K., Cruz, K. L., Rice, E. L., & Riedel, A. 2014, in IAU Symposium, Vol. 299, IAU Symposium, ed. M. Booth, B. C. Matthews, & J. R. Graham, 36–37

Fegley, Jr., B., & Lodders, K. 1996, ApJ, 472, L37

Filippazzo, J. C., Rice, E. L., Faherty, J., Cruz, K. L., Van Gordon, M. M., & Looper, D. L. 2015, ApJ, 810, 158

Forgan, D., & Rice, K. 2013, MNRAS, 432, 3168

Fortney, J. J. 2012, ApJ, 747, L27

Freedman, R. S., Marley, M. S., & Lodders, K. 2008, ApJS, 174, 504

Freytag, B., Allard, F., Ludwig, H.-G., Homeier, D., & Steffen, M. 2010, A&A, 513, A19

Gagné, J., Lafrenière, D., Doyon, R., Malo, L., & Artigau, É. 2014, ApJ, 783, 121

Gagné, J., et al. 2015, ApJS, 219, 33

Gizis, J., & Reid, I. N. 1995, AJ, 110, 1248

Goldman, B., Pitann, J., Zapatero Osorio, M. R., Bailer-Jones, C. A. L., Béjar, V. J. S., Caballero, J. A., & Henning, T. 2009, A&A, 502, 929

Gray, R. O., Corbally, C. J., Garrison, R. F., McFadden, M. T., & Robinson, P. E. 2003, AJ, 126, 2048

Gustafsson, B., Edvardsson, B., Eriksson, K., Jørgensen, U. G., Nordlund, Å., & Plez, B. 2008, A&A, 486, 951

Hansen, C. J., et al. 2011, A&A, 527, A65

—. 2012, A&A, 545, A31

Hayashi, C., & Nakano, T. 1963, Prog. of T. Ph., 30, 460

Helling, C., & Woitke, P. 2006, A&A, 455, 325

Helling, C., Woitke, P., Rimmer, P. B., Kamp, I., Thi, W.-F., & Meijerink, R. 2014, Life, 4

Helling, C., Woitke, P., & Thi, W.-F. 2008, A&A, 485, 547

Henden, A. A., Levine, S., Terrell, D., & Welch, D. L. 2015, in American Astronomical Society Meeting Abstracts, Vol. 225, American Astronomical Society Meeting Abstracts, 336.16

Hormuth, F., Hippler, S., Brandner, W., Wagner, K., & Henning, T. 2008, in Proc. SPIE, Vol. 7014, Ground-based and Airborne Instrumentation for Astronomy II, 701448

Johnson, J. A., Aller, K. M., Howard, A. W., & Crepp, J. R. 2010, PASP, 122, 905

Johnson, J. A., & Apps, K. 2009, ApJ, 699, 933

Kirkpatrick, J. D. 2005, ARA&A, 43, 195

Kirkpatrick, J. D., Cushing, M. C., Gelino, C. R., Beichman, C. A., Tinney, C. G., Faherty, J. K., Schneider, A., & Mace, G. N. 2013, ApJ, 776, 128

Kirkpatrick, J. D., et al. 2012, ApJ, 753, 156

Kley, W., & Nelson, R. P. 2012, ARA&A, 50, 211

Konopacky, Q. M., Barman, T. S., Macintosh, B. A., & Marois, C. 2013, Science, 339, 1398

Kopytova, T. G., Brandner, W., Tognelli, E., Prada Moroni, P. G., Da Rio, N., Röser, S., & Schilbach, E. 2016, A&A, 585, A7

Kopytova, T. G., et al. 2014, ApJ, 797, 3

Kumar, S. S. 1963, ApJ, 137, 1121

Kupka, F. G., Ryabchikova, T. A., Piskunov, N. E., Stempels, H. C., & Weiss, W. W. 2000, Baltic Astronomy, 9, 590

Lambrechts, M., & Johansen, A. 2012, A&A, 544, A32

LeBlanc, F. 2010, An Introduction to Stellar Astrophysics

Leggett, S. K., Morley, C. V., Marley, M. S., Saumon, D., Fortney, J. J., & Visscher, C. 2013, ApJ, 763, 130

Leggett, S. K., Saumon, D., Marley, M. S., Geballe, T. R., Golimowski, D. A., Stephens, D., & Fan, X. 2007, ApJ, 655, 1079

Li, L., et al. 2012, Journal of Geophysical Research (Planets), 117, 11002

Line, M. R., Knutson, H., Wolf, A. S., & Yung, Y. L. 2014, ApJ, 783, 70

Line, M. R., Teske, J., Burningham, B., Fortney, J. J., & Marley, M. S. 2015, ApJ, 807, 183

Liu, M. C., Dupuy, T. J., Bowler, B. P., Leggett, S. K., & Best, W. M. J. 2012, ApJ, 758, 57

Liu, M. C., et al. 2013, ApJ, 777, L20

Lodders, K. 1999, ApJ, 519, 793

—. 2003, ApJ, 591, 1220

Lodders, K., & Fegley, B. 2002, Icarus, 155, 393

Lodders, K., & Fegley, Jr., B. 2006, Chemistry of Low Mass Substellar Objects, ed. J. W. Mason, 1

Luhman, K. L. 2014, ApJ, 786, L18

Luhman, K. L., & Esplin, T. L. 2014, ArXiv e-prints

—. 2016, ArXiv e-prints

Lunine, J. I., Hubbard, W. B., & Marley, M. S. 1986, ApJ, 310, 238

Macintosh, B., et al. 2015, Science, 350, 64

Magnier, E. A., et al. 2013, ApJS, 205, 20

Manjavacas, E., et al. 2014, A&A, 564, A55

Marboeuf, U., Thiabaud, A., Alibert, Y., Cabral, N., & Benz, W. 2014a, A&A, 570, A36

—. 2014b, A&A, 570, A35

Marley, M. S., Saumon, D., & Goldblatt, C. 2010, ApJ, 723, L117

Marocco, F., et al. 2014, MNRAS, 439, 372

Marois, C., Macintosh, B., Barman, T., Zuckerman, B., Song, I., Patience, J., Lafrenière, D., & Doyon, R. 2008, Science, 322, 1348

Marois, C., Zuckerman, B., Konopacky, Q. M., Macintosh, B., & Barman, T. 2010, Nature, 468, 1080

Martin, C., & GALEX Team. 2005, in IAU Symposium, Vol. 216, Maps of the Cosmos, ed. M. Colless, L. Staveley-Smith, & R. A. Stathakis, 221

Mason, B. D., Wycoff, G. L., Hartkopf, W. I., Douglass, G. G., & Worley, C. E. 2001, AJ, 122, 3466

Mayor, M., et al. 2011, ArXiv e-prints

Mermilliod, J.-C., Mayor, M., & Udry, S. 2009, A&A, 498, 949

Metchev, S. A., et al. 2015, ApJ, 799, 154

Miglio, A., et al. 2012, MNRAS, 419, 2077

Mollière, P., van Boekel, R., Dullemond, C., Henning, T., & Mordasini, C. 2015, ApJ, 813, 47

Mordasini, C., Alibert, Y., Benz, W., Klahr, H., & Henning, T. 2012, A&A, 541, A97

Mordasini, C., Alibert, Y., Benz, W., & Naef, D. 2009, A&A, 501, 1161

Morley, C. V., Fortney, J. J., Marley, M. S., Visscher, C., Saumon, D., & Leggett, S. K. 2012, ApJ, 756, 172

Morley, C. V., Marley, M. S., Fortney, J. J., Lupu, R., Saumon, D., Greene, T., & Lodders, K. 2014, ApJ, 787, 78

Morzinski, K. M. 2011, PhD thesis, University of California, Santa Cruz

Nakajima, T., Oppenheimer, B. R., Kulkarni, S. R., Golimowski, D. A., Matthews, K., & Durrance, S. T. 1995, Nature, 378, 463

Ness, M., Hogg, D. W., Rix, H.-W., Ho, A. Y. Q., & Zasowski, G. 2015, ApJ, 808, 16

Öberg, K. I., Murray-Clay, R., & Bergin, E. A. 2011, ApJ, 743, L16

Oppenheimer, B. R., Kulkarni, S. R., Matthews, K., & Nakajima, T. 1995, Science, 270, 1478

Patience, J., Ghez, A. M., Reid, I. N., Weinberger, A. J., & Matthews, K. 1998, AJ, 115, 1972

Patience, J., King, R. R., De Rosa, R. J., Vigan, A., Witte, S., Rice, E., Helling, C., & Hauschildt, P. 2012, A&A, 540, A85

Percival, S. M., Salaris, M., & Groenewegen, M. A. T. 2005, A&A, 429, 887

Perryman, M. A. C., et al. 1998, A&A, 331, 81

Pollack, J. B., Hubickyj, O., Bodenheimer, P., Lissauer, J. J., Podolak, M., & Greenzweig, Y. 1996, Icarus, 124, 62

Radigan, J., Lafrenière, D., Jayawardhana, R., & Artigau, E. 2014, ApJ, 793, 75

Rafikov, R. R. 2011, ApJ, 727, 86

Rameau, J., et al. 2013, ApJ, 779, L26

Rayner, J. T., Cushing, M. C., & Vacca, W. D. 2009, ApJS, 185, 289

Rebolo, R., Zapatero Osorio, M. R., & Martín, E. L. 1995, Nature, 377, 129

Reid, I. N., & Gizis, J. E. 1997, AJ, 114, 1992

Reid, I. N., & Mahoney, S. 2000, MNRAS, 316, 827

Rice, J. B., Wehlau, W. H., & Khokhlova, V. L. 1989, A&A, 208, 179

Richard, C., et al. 2012, J. Quant. Spec. Radiat. Transf., 113, 1276

Röser, S., Schilbach, E., Piskunov, A. E., Kharchenko, N. V., & Scholz, R.-D. 2011, A&A, 531, A92

Rossow, W. B. 1978, Icarus, 36, 1

Saumon, D., & Marley, M. S. 2008, ApJ, 689, 1327

Schlafly, E. F., & Finkbeiner, D. P. 2011, ApJ, 737, 103

Schlafly, E. F., et al. 2012, ApJ, 756, 158

Schneider, A. C., Cushing, M. C., Kirkpatrick, J. D., & Gelino, C. R. 2016, ApJ, 823, L35

Skemer, A., et al. 2016, ArXiv e-prints

Skemer, A. J., et al. 2014, ApJ, 792, 17

Skrutskie, M. F., et al. 2006, AJ, 131, 1163

Sneden, C. A. 1973, PhD thesis, THE UNIVERSITY OF TEXAS AT AUSTIN.

Snellen, I. A. G., Brandl, B. R., de Kok, R. J., Brogi, M., Birkby, J., & Schwarz, H. 2014, Nature, 509, 63

Stamatellos, D., & Whitworth, A. P. 2009, MNRAS, 392, 413

Stern, R. A., Schmitt, J. H. M. M., & Kahabka, P. T. 1995, ApJ, 448, 683

Sudarsky, D., Burrows, A., & Hubeny, I. 2003, ApJ, 588, 1121

Thiabaud, A., Marboeuf, U., Alibert, Y., Cabral, N., Leya, I., & Mezger, K. 2014, A&A, 562, A27

Thiabaud, A., Marboeuf, U., Alibert, Y., Leya, I., & Mezger, K. 2015, A&A, 574, A138

Tinney, C. G., Faherty, J. K., Kirkpatrick, J. D., Wright, E. L., Gelino, C. R., Cushing, M. C., Griffith, R. L., & Salter, G. 2012, ApJ, 759, 60

Tody, D. 1993, in Astronomical Society of the Pacific Conference Series, Vol. 52, Astronomical Data Analysis Software and Systems II, ed. R. J. Hanisch, R. J. V. Brissenden, & J. Barnes, 173

Tognelli, E., Degl'Innocenti, S., & Prada Moroni, P. G. 2012, A&A, 548, A41

Tognelli, E., Prada Moroni, P. G., & Degl'Innocenti, S. 2011, A&A, 533, A109

Tonry, J. L., et al. 2012, ApJ, 750, 99

Torres, C. A. O., Quast, G. R., da Silva, L., de La, R. R., Melo, C. H. F., & Sterzik, M. 2006, VizieR Online Data Catalog, 346

Tremblin, P., Amundsen, D. S., Chabrier, G., Baraffe, I., Drummond, B., Hinkley, S., Mourier, P., & Venot, O. 2016, ApJ, 817, L19

Tremblin, P., Amundsen, D. S., Mourier, P., Baraffe, I., Chabrier, G., Drummond, B., Homeier, D., & Venot, O. 2015, ApJ, 804, L17

Valenti, J. A., & Fischer, D. A. 2005, in Protostars and Planets V Posters, Vol. 1286, 8592

van Leeuwen, F. 2007, A&A, 474, 653

—. 2009, A&A, 497, 209

Visscher, C., Lodders, K., & Fegley, Jr., B. 2006, ApJ, 648, 1181

—. 2010, ApJ, 716, 1060

Vogt, S. S., Penrod, G. D., & Hatzes, A. P. 1987, ApJ, 321, 496

Wilson, P. A., Rajan, A., & Patience, J. 2014, A&A, 566, A111

Wright, E. L., et al. 2010, AJ, 140, 1868

—. 2014, ArXiv e-prints

Yurchenko, S. N., Barber, R. J., & Tennyson, J. 2011, MNRAS, 413, 1828

Zapatero Osorio, M. R., et al. 2016, ArXiv e-prints

Zhou, Y., Apai, D., Schneider, G. H., Marley, M. S., & Showman, A. P. 2016, ApJ, 818, 176

# Chapter A

# Single-star sequence in the Hyades

In this Appendix I present the complete table containing absolute $JHK_s$ (2MASS) photometry and physical parameters of the Hyades single-star sequence (more details in Chapter 2 and Kopytova et al. 2016).

Table A.1: Absolute $JHK_s$(2MASS) photometry and physical parameters of the Hyades single-star sequence members. The "Resolution" column correspond to values outside which no companion was detected. Objects observed only by the spectroscopic survey of Mermilliod et al. (2009) have no resolution value. Hyades IDs are from Röser et al. (2011).

| Hyades ID | parallax [mas] | parallax error [mas] | $M_J$ | $dM_J$ | $M_H$ | $dM_H$ | $M_K$ | $dM_K$ | $T_{eff}$ [K] | log($g$) (cgs) | Mass [M⊙] | Resolution [AU] |
|---|---|---|---|---|---|---|---|---|---|---|---|---|
| 3 | 28.1 | 1.08 | 7.32 | 0.09 | 6.72 | 0.09 | 6.50 | 0.09 | 3500 | 4.90 | 0.38 | 3.91 |
| 6 | 31.9 | 0.1 | 3.64 | 0.02 | 3.37 | 0.02 | 3.30 | 0.02 | 5883 | 4.48 | 1.06 | 3.45 |
| 9 | 22.36 | 0.41 | 7.03 | 0.05 | 6.48 | 0.05 | 6.21 | 0.05 | 3569 | 4.87 | 0.43 | 4.92 |
| 10 | 23.23 | 0.41 | 6.62 | 0.05 | 6.04 | 0.04 | 5.78 | 0.04 | 3701 | 4.80 | 0.49 | 4.74 |
| 11 | 23.41 | 0.37 | 5.84 | 0.04 | 5.16 | 0.06 | 4.99 | 0.04 | 4089 | 4.70 | 0.62 | 4.70 |
| 13 | 34 | 0.36 | 7.37 | 0.03 | 6.76 | 0.03 | 6.50 | 0.03 | 3495 | 4.91 | 0.38 | 3.24 |
| 16 | 19.73 | 0.13 | 4.55 | 0.07 | 4.16 | 0.04 | 4.03 | 0.02 | 5076 | 4.60 | 0.84 | 5.58 |
| 21 | 19.46 | 0.4 | 6.11 | 0.05 | 5.49 | 0.05 | 5.29 | 0.05 | 3924 | 4.73 | 0.57 | 5.65 |
| 22 | 23.5 | 0.4 | 7.70 | 0.04 | 7.12 | 0.04 | 6.82 | 0.04 | 3428 | 4.95 | 0.33 | 4.68 |
| 25 | 26.37 | 0.16 | 2.99 | 0.03 | 2.79 | 0.04 | 2.68 | 0.03 | 6412 | 4.35 | 1.24 | 4.17 |
| 27 | 24.58 | 0.13 | 4.34 | 0.03 | 3.95 | 0.02 | 3.86 | 0.03 | 5287 | 4.57 | 0.89 | 4.48 |
| 28 | 30.89 | 0.04 | 2.76 | 0.20 | 2.26 | 0.04 | 2.23 | 0.02 | 6933 | 4.25 | 1.42 | 3.56 |
| 30 | 30.26 | 0.42 | 7.82 | 0.04 | 7.18 | 0.03 | 6.92 | 0.04 | 3412 | 4.97 | 0.31 | 3.64 |
| 34 | 19.24 | 0.45 | 7.26 | 0.06 | 6.67 | 0.06 | 6.44 | 0.05 | 3514 | 4.90 | 0.39 | 5.72 |
| 37 | 27.85 | 0.44 | 8.15 | 0.04 | 7.58 | 0.04 | 7.29 | 0.04 | 3340 | 5.00 | 0.26 | 3.95 |
| 39 | 21.35 | 0.15 | 6.62 | 0.03 | 5.98 | 0.03 | 5.73 | 0.03 | 3713 | 4.80 | 0.50 | 5.15 |
| 40 | 25.36 | 0.14 | 3.85 | 0.03 | 3.58 | 0.03 | 3.48 | 0.03 | 5713 | 4.51 | 1.00 | 4.34 |
| 43 | 29.08 | 0.43 | 6.63 | 0.04 | 5.95 | 0.04 | 5.73 | 0.04 | 3715 | 4.80 | 0.50 | 3.78 |
| 49 | 22.27 | 0.44 | 6.04 | 0.05 | 5.37 | 0.05 | 5.17 | 0.05 | 3977 | 4.72 | 0.59 | 4.94 |
| 50 | 30.63 | 0.55 | 5.66 | 0.05 | 5.00 | 0.05 | 4.83 | 0.04 | 4198 | 4.68 | 0.65 | 3.59 |
| 51 | 16.64 | 0.18 | 3.94 | 0.03 | 3.60 | 0.03 | 3.50 | 0.04 | 5662 | 4.52 | 0.99 | 6.61 |

Table A.1: continued.

| Hyades ID | parallax [mas] | parallax error [mas] | $M_J$ | $dM_J$ | $M_H$ | $dM_H$ | $M_K$ | $dM_K$ | $T_{eff}$ [K] | log($g$) (cgs) | Mass [$M\odot$] | Resolution [AU] |
|---|---|---|---|---|---|---|---|---|---|---|---|---|
| 52 | 32.16 | 0.2 | 5.08 | 0.03 | 4.49 | 0.05 | 4.42 | 0.03 | 4615 | 4.64 | 0.74 | 3.42 |
| 53 | 31.71 | 0.45 | 5.75 | 0.04 | 5.10 | 0.05 | 4.92 | 0.04 | 4136 | 4.69 | 0.63 | 3.47 |
| 57 | 26.66 | 0.5 | 7.19 | 0.05 | 6.58 | 0.05 | 6.33 | 0.05 | 3536 | 4.88 | 0.41 | 4.13 |
| 61 | 19.7 | 0.11 | 2.83 | 0.02 | 2.62 | 0.02 | 2.58 | 0.02 | 6533 | 4.33 | 1.28 | 5.58 |
| 65 | 27.08 | 0.21 | 6.72 | 0.03 | 6.12 | 0.03 | 5.86 | 0.03 | 3671 | 4.82 | 0.48 | 4.06 |
| 66 | 25.81 | 0.48 | 6.16 | 0.05 | 5.53 | 0.05 | 5.29 | 0.04 | 3908 | 4.74 | 0.57 | 4.26 |
| 70 | 28.1 | 0.5 | 7.81 | 0.04 | 7.21 | 0.04 | 6.96 | 0.04 | 3409 | 4.97 | 0.31 | 3.91 |
| 71 | 18.85 | 0.2 | 5.12 | 0.04 | 4.53 | 0.05 | 4.43 | 0.03 | 4589 | 4.64 | 0.73 | 5.84 |
| 73 | 24.14 | 0.48 | 6.95 | 0.05 | 6.33 | 0.05 | 6.08 | 0.05 | 3602 | 4.85 | 0.45 | 4.56 |
| 74 | 24.81 | 1.5 | 6.68 | 0.13 | 6.08 | 0.13 | 5.84 | 0.13 | 3681 | 4.81 | 0.49 | 4.43 |
| 77 | 27.2 | 0.48 | 7.94 | 0.04 | 7.33 | 0.05 | 7.08 | 0.05 | 3385 | 4.98 | 0.29 | 4.04 |
| 78 | 21.82 | 0.49 | 7.18 | 0.05 | 6.53 | 0.05 | 6.31 | 0.05 | 3543 | 4.88 | 0.41 | 5.04 |
| 79 | 18.1 | 0.56 | 7.09 | 0.07 | 6.52 | 0.07 | 6.27 | 0.07 | 3555 | 4.87 | 0.42 | 6.08 |
| 82 | 26.12 | 0.49 | 6.89 | 0.05 | 6.31 | 0.05 | 6.03 | 0.04 | 3616 | 4.84 | 0.45 | 4.21 |
| 83 | 21.12 | 0.22 | 4.40 | 0.03 | 4.02 | 0.06 | 3.87 | 0.03 | 5243 | 4.58 | 0.88 | 5.21 |
| 85 | 24.25 | 0.43 | 5.03 | 0.04 | 4.46 | 0.04 | 4.32 | 0.04 | 4678 | 4.63 | 0.75 | 2.47 |
| 86 | 22.17 | 0.25 | 5.43 | 0.04 | 4.77 | 0.04 | 4.62 | 0.04 | 4362 | 4.66 | 0.68 | 4.96 |
| 88 | 23.83 | 0.06 | 2.14 | 0.03 | 2.05 | 0.04 | 1.98 | 0.02 | 7311 | 4.22 | 1.54 | 4.62 |
| 89 | 14.21 | 0.24 | 4.25 | 0.04 | 3.83 | 0.04 | 3.80 | 0.04 | 5381 | 4.56 | 0.91 | 7.74 |
| 93 | 22.31 | 0.54 | 6.70 | 0.06 | 6.11 | 0.06 | 5.80 | 0.06 | 3681 | 4.81 | 0.48 | 4.93 |
| 94 | 21.26 | 0.36 | 4.82 | 0.04 | 4.33 | 0.04 | 4.21 | 0.04 | 4847 | 4.62 | 0.79 | 5.17 |
| 95 | 24.69 | 0.23 | 4.38 | 0.03 | 4.00 | 0.03 | 3.87 | 0.03 | 5252 | 4.58 | 0.88 | 2.43 |
| 97 | 17.49 | 1.43 | 6.79 | 0.18 | 6.14 | 0.18 | 5.92 | 0.18 | 3653 | 4.82 | 0.47 | 6.29 |

Table A.1: continued.

| Hyades ID | parallax [mas] | parallax error [mas] | $M_J$ | $dM_J$ | $M_H$ | $dM_H$ | $M_K$ | $dM_K$ | $T_{eff}$ [K] | log($g$) (cgs) | Mass [M⊙] | Resolution [AU] |
|---|---|---|---|---|---|---|---|---|---|---|---|---|
| 99 | 21.91 | 0.52 | 6.93 | 0.06 | 6.33 | 0.06 | 6.09 | 0.06 | 3602 | 4.85 | 0.45 | 5.02 |
| 100 | 20.96 | 0.51 | 6.40 | 0.06 | 5.79 | 0.06 | 5.55 | 0.06 | 3792 | 4.77 | 0.53 | 5.25 |
| 101 | 22 | 0.49 | 7.69 | 0.05 | 7.10 | 0.05 | 6.81 | 0.05 | 3430 | 4.95 | 0.33 | 5.00 |
| 104 | 22.68 | 0.61 | 8.62 | 0.06 | 8.03 | 0.06 | 7.77 | 0.06 | 3254 | 5.05 | 0.21 | 2.20 |
| 105 | 21.31 | 0.49 | 7.27 | 0.05 | 6.66 | 0.05 | 6.42 | 0.05 | 3516 | 4.90 | 0.39 | 5.16 |
| 106 | 13.46 | 0.2 | 3.37 | 0.04 | 3.09 | 0.04 | 3.02 | 0.04 | 6116 | 4.42 | 1.13 | 8.17 |
| 107 | 19.84 | 0.49 | 6.84 | 0.06 | 6.24 | 0.06 | 5.99 | 0.06 | 3631 | 4.83 | 0.46 | 5.54 |
| 108 | 23.2 | 1.49 | 5.54 | 0.14 | 4.89 | 0.14 | 4.71 | 0.14 | 4278 | 4.67 | 0.67 | 4.74 |
| 109 | 25.42 | 0.51 | 6.56 | 0.05 | 5.94 | 0.05 | 5.73 | 0.05 | 3726 | 4.79 | 0.50 | 4.33 |
| 112 | 22.17 | 0.51 | 6.60 | 0.05 | 5.97 | 0.05 | 5.73 | 0.05 | 3716 | 4.80 | 0.50 | 4.96 |
| 114 | 24.07 | 0.22 | 2.47 | 0.03 | 2.30 | 0.04 | 2.23 | 0.03 | 6875 | 4.26 | 1.40 | 4.57 |
| 116 | 21.03 | 0.53 | 8.19 | 0.06 | 7.58 | 0.06 | 7.31 | 0.06 | 3336 | 5.01 | 0.26 | 2.38 |
| 118 | 22.24 | 0.05 | 1.97 | 0.02 | 1.81 | 0.03 | 1.78 | 0.02 | 7600 | 4.19 | 1.64 | 4.95 |
| 120 | 21.97 | 0.21 | 4.75 | 0.03 | 4.26 | 0.05 | 4.16 | 0.03 | 4920 | 4.61 | 0.81 | 5.01 |
| 123 | 23.25 | 0.54 | 7.60 | 0.05 | 7.01 | 0.05 | 6.75 | 0.05 | 3443 | 4.94 | 0.34 | 2.15 |
| 124 | 20.56 | 0.46 | 7.55 | 0.05 | 6.96 | 0.05 | 6.69 | 0.05 | 3455 | 4.93 | 0.35 | 5.35 |
| 128 | 19.97 | 0.59 | 8.42 | 0.07 | 7.84 | 0.07 | 7.56 | 0.07 | 3289 | 5.03 | 0.23 | 2.50 |
| 133 | 21.5 | 0.77 | 5.55 | 0.08 | 4.92 | 0.08 | 4.77 | 0.08 | 4256 | 4.68 | 0.66 | 2.79 |
| 134 | 22.28 | 0.24 | 4.49 | 0.04 | 4.10 | 0.04 | 3.99 | 0.03 | 5135 | 4.59 | 0.85 | 2.69 |
| 136 | 25.16 | 0.54 | 6.49 | 0.05 | 5.82 | 0.05 | 5.60 | 0.05 | 3770 | 4.78 | 0.52 | 4.37 |
| 137 | 21.04 | 0.19 | 3.37 | 0.03 | 3.15 | 0.04 | 3.06 | 0.03 | 6095 | 4.43 | 1.12 | 5.23 |
| 138 | 20.45 | 0.53 | 7.89 | 0.06 | 7.31 | 0.06 | 7.02 | 0.06 | 3393 | 4.98 | 0.30 | 2.44 |
| 139 | 20.11 | 0.21 | 6.50 | 0.03 | 5.78 | 0.04 | 5.61 | 0.03 | 3774 | 4.78 | 0.52 | 5.47 |

Table A.1: continued.

| Hyades ID | parallax [mas] | parallax error [mas] | $M_J$ | $dM_J$ | $M_H$ | $dM_H$ | $M_K$ | $dM_K$ | $T_{eff}$ [K] | log($g$) (cgs) | Mass [M⊙] | Resolution [AU] |
|---|---|---|---|---|---|---|---|---|---|---|---|---|
| 140 | 22.47 | 0.35 | 5.12 | 0.04 | 4.57 | 0.06 | 4.42 | 0.04 | 4581 | 4.64 | 0.73 | 4.90 |
| 141 | 29.42 | 0.56 | 8.79 | 0.05 | 8.20 | 0.05 | 7.90 | 0.05 | 3227 | 5.07 | 0.19 | 1.70 |
| 145 | 23.76 | 1.37 | 5.65 | 0.13 | 4.99 | 0.13 | 4.81 | 0.13 | 4208 | 4.68 | 0.65 | 2.53 |
| 146 | 17.83 | 0.2 | 3.44 | 0.04 | 3.00 | 0.05 | 2.90 | 0.04 | 6159 | 4.41 | 1.15 | 6.17 |
| 147 | 20.92 | 0.47 | 5.42 | 0.06 | 4.77 | 0.06 | 4.65 | 0.06 | 4357 | 4.67 | 0.68 | 2.87 |
| 148 | 21.63 | 0.24 | 4.52 | 0.03 | 4.12 | 0.03 | 4.00 | 0.03 | 5117 | 4.59 | 0.85 | 2.77 |
| 152 | 28.29 | 0.29 | 5.17 | 0.03 | 4.60 | 0.03 | 4.52 | 0.03 | 4523 | 4.65 | 0.72 | 3.89 |
| 153 | 28.3 | 0.62 | 9.34 | 0.05 | 8.72 | 0.06 | 8.41 | 0.05 | 3128 | 5.13 | 0.15 | 1.77 |
| 155 | 22.51 | 0.09 | 2.56 | 0.02 | 2.39 | 0.02 | 2.33 | 0.02 | 6778 | 4.28 | 1.37 | 4.89 |
| 157 | 21.6 | 0.54 | 7.27 | 0.06 | 6.69 | 0.06 | 6.42 | 0.06 | 3513 | 4.90 | 0.39 | 5.09 |
| 159 | 26.83 | 0.11 | 2.21 | 0.02 | 2.14 | 0.12 | 1.96 | 0.02 | 7229 | 4.22 | 1.52 | 4.10 |
| 165 | 27.65 | 0.56 | 6.94 | 0.05 | 6.30 | 0.05 | 6.08 | 0.05 | 3606 | 4.85 | 0.45 | 3.98 |
| 167 | 25.57 | 0.66 | 9.17 | 0.06 | 8.53 | 0.06 | 8.27 | 0.06 | 3163 | 5.11 | 0.16 | 1.96 |
| 168 | 23.12 | 0.81 | 7.76 | 0.08 | 7.22 | 0.08 | 6.94 | 0.08 | 3412 | 4.97 | 0.31 | 4.76 |
| 174 | 21.73 | 0.24 | 3.54 | 0.03 | 3.29 | 0.03 | 3.22 | 0.03 | 5959 | 4.46 | 1.08 | 2.76 |
| 175 | 20.48 | 0.58 | 6.85 | 0.06 | 6.27 | 0.07 | 5.98 | 0.06 | 3628 | 4.84 | 0.46 | 5.37 |
| 176 | 17.87 | 0.09 | 2.47 | 0.02 | 2.34 | 0.03 | 2.27 | 0.02 | 6849 | 4.26 | 1.39 | 6.16 |
| 177 | 22.91 | 0.17 | 3.68 | 0.03 | 3.40 | 0.03 | 3.32 | 0.03 | 5861 | 4.48 | 1.05 | 2.62 |
| 178 | 22.19 | 0.13 | 2.86 | 0.02 | 2.65 | 0.02 | 2.59 | 0.02 | 6512 | 4.33 | 1.27 | 4.96 |
| 179 | 18.05 | 0.61 | 8.16 | 0.08 | 7.54 | 0.08 | 7.27 | 0.08 | 3343 | 5.00 | 0.26 | 2.77 |
| 183 | 22 | 0.55 | 5.62 | 0.06 | 4.97 | 0.09 | 4.72 | 0.06 | 4243 | 4.68 | 0.66 | 5.00 |
| 184 | 22.33 | 0.77 | 5.69 | 0.08 | 5.04 | 0.08 | 4.87 | 0.08 | 4173 | 4.69 | 0.64 | 2.69 |
| 187 | 39.21 | 0.58 | 8.75 | 0.04 | 8.18 | 0.04 | 7.88 | 0.04 | 3231 | 5.07 | 0.19 | 2.81 |

Table A.1: continued.

| Hyades ID | parallax [mas] | parallax error [mas] | $M_J$ | $dM_J$ | $M_H$ | $dM_H$ | $M_K$ | $dM_K$ | $T_{eff}$ [K] | log($g$) (cgs) | Mass [M$\odot$] | Resolution [AU] |
|---|---|---|---|---|---|---|---|---|---|---|---|---|
| 190 | 21.8 | 0.11 | 2.21 | 0.04 | 2.09 | 0.03 | 2.02 | 0.02 | 7223 | 4.22 | 1.51 | 5.05 |
| 192 | 22.55 | 0.59 | 7.57 | 0.06 | 6.96 | 0.06 | 6.68 | 0.06 | 3454 | 4.93 | 0.35 | 4.88 |
| 193 | 21.57 | 0.56 | 6.92 | 0.06 | 6.32 | 0.06 | 6.08 | 0.06 | 3607 | 4.85 | 0.45 | 5.10 |
| 194 | 22.4 | 0.7 | 9.20 | 0.07 | 8.60 | 0.07 | 8.33 | 0.07 | 3152 | 5.12 | 0.15 | 2.23 |
| 195 | 22.58 | 0.4 | 5.83 | 0.04 | 5.22 | 0.04 | 5.04 | 0.04 | 4070 | 4.70 | 0.61 | 2.66 |
| 198 | 19.85 | 0.23 | 4.19 | 0.03 | 3.86 | 0.03 | 3.76 | 0.03 | 5408 | 4.56 | 0.92 | 3.02 |
| 201 | 21.27 | 0.59 | 7.07 | 0.06 | 6.45 | 0.06 | 6.22 | 0.06 | 3566 | 4.87 | 0.43 | 5.17 |
| 202 | 21.31 | 0.24 | 5.24 | 0.03 | 4.64 | 0.03 | 4.55 | 0.03 | 4477 | 4.65 | 0.71 | 2.82 |
| 203 | 19.89 | 0.64 | 6.96 | 0.07 | 6.36 | 0.07 | 6.11 | 0.07 | 3594 | 4.85 | 0.44 | 5.53 |
| 204 | 23.78 | 0.57 | 7.80 | 0.06 | 7.23 | 0.06 | 6.95 | 0.06 | 3409 | 4.97 | 0.31 | 4.63 |
| 210 | 19.06 | 0.64 | 7.27 | 0.08 | 6.68 | 0.08 | 6.42 | 0.07 | 3514 | 4.90 | 0.39 | 5.77 |
| 213 | 21.17 | 0.58 | 8.28 | 0.06 | 7.71 | 0.06 | 7.39 | 0.06 | 3317 | 5.02 | 0.25 | 2.36 |
| 216 | 22.67 | 0.43 | 4.66 | 0.05 | 4.20 | 0.05 | 4.10 | 0.04 | 4993 | 4.61 | 0.82 | 2.65 |
| 223 | 21.79 | 0.65 | 5.81 | 0.07 | 5.17 | 0.07 | 4.99 | 0.07 | 4092 | 4.70 | 0.62 | 5.05 |
| 225 | 22.03 | 0.29 | 4.00 | 0.03 | 3.72 | 0.03 | 3.64 | 0.03 | 5569 | 4.54 | 0.96 | 4.99 |
| 226 | 24.01 | 0.59 | 7.81 | 0.06 | 7.19 | 0.06 | 6.91 | 0.06 | 3413 | 4.97 | 0.31 | 4.58 |
| 227 | 21.89 | 0.18 | 3.84 | 0.03 | 3.57 | 0.03 | 3.49 | 0.02 | 5713 | 4.51 | 1.00 | 2.74 |
| 228 | 20.08 | 0.56 | 6.62 | 0.06 | 5.96 | 0.06 | 5.74 | 0.06 | 3715 | 4.80 | 0.50 | 5.48 |
| 229 | 22.33 | 0.08 | -1.29 | 0.25 | -1.76 | 0.21 | -1.74 | 0.20 | 6062 | 3.24 | 2.30 | 4.93 |
| 233 | 22.39 | 0.15 | 3.15 | 0.02 | 2.93 | 0.03 | 2.87 | 0.02 | 6265 | 4.39 | 1.18 | 4.91 |
| 234 | 23.82 | 0.11 | 2.23 | 0.02 | 2.09 | 0.03 | 2.04 | 0.02 | 7173 | 4.23 | 1.50 | 4.62 |
| 237 | 21.14 | 0.09 | 1.38 | 0.05 | 1.60 | 0.28 | 1.31 | 0.02 | 8140 | 4.08 | 1.90 | 5.20 |
| 242 | 21.63 | 0.74 | 8.04 | 0.08 | 7.43 | 0.08 | 7.16 | 0.08 | 3367 | 4.99 | 0.28 | 2.31 |

Table A.1: continued.

| Hyades ID | parallax [mas] | parallax error [mas] | $M_J$ | $dM_J$ | $M_H$ | $dM_H$ | $M_K$ | $dM_K$ | $T_{eff}$ [K] | log($g$) (cgs) | Mass [$M_\odot$] | Resolution [AU] |
|---|---|---|---|---|---|---|---|---|---|---|---|---|
| 244 | 20.5 | 0.11 | 2.53 | 0.02 | 2.34 | 0.02 | 2.32 | 0.02 | 6809 | 4.27 | 1.38 | 5.37 |
| 245 | 21.61 | 0.13 | 2.62 | 0.02 | 2.47 | 0.02 | 2.42 | 0.02 | 6703 | 4.29 | 1.34 | 5.09 |
| 246 | 20.5 | 0.12 | 2.34 | 0.03 | 2.22 | 0.04 | 2.15 | 0.02 | 7021 | 4.25 | 1.45 | 5.37 |
| 247 | 20.64 | 0.69 | 7.87 | 0.08 | 7.26 | 0.08 | 7.01 | 0.07 | 3399 | 4.98 | 0.30 | 2.42 |
| 248 | 25.75 | 0.86 | 7.84 | 0.08 | 7.25 | 0.08 | 6.97 | 0.07 | 3404 | 4.97 | 0.31 | 1.94 |
| 249 | 25.78 | 0.65 | 8.57 | 0.06 | 7.96 | 0.06 | 7.69 | 0.06 | 3267 | 5.05 | 0.21 | 1.94 |
| 250 | 20.89 | 1.07 | 7.19 | 0.11 | 6.61 | 0.11 | 6.34 | 0.11 | 3533 | 4.89 | 0.41 | 5.27 |
| 251 | 27.16 | 0.58 | 7.05 | 0.05 | 6.39 | 0.05 | 6.15 | 0.05 | 3579 | 4.86 | 0.43 | 4.05 |
| 256 | 18.65 | 0.68 | 7.13 | 0.08 | 6.49 | 0.08 | 6.27 | 0.08 | 3554 | 4.87 | 0.42 | 2.68 |
| 257 | 27.21 | 1.78 | 6.78 | 0.14 | 6.14 | 0.14 | 5.90 | 0.14 | 3658 | 4.82 | 0.47 | 2.21 |
| 258 | 20.78 | 0.65 | 7.05 | 0.07 | 6.42 | 0.07 | 6.16 | 0.07 | 3577 | 4.86 | 0.43 | 5.29 |
| 261 | 21.1 | 0.15 | -1.28 | 0.25 | -1.80 | 0.20 | -1.74 | 0.23 | 6062 | 3.24 | 2.30 | 5.21 |
| 265 | 21.93 | 0.7 | 7.95 | 0.07 | 7.34 | 0.07 | 7.06 | 0.07 | 3385 | 4.98 | 0.29 | 2.28 |
| 269 | 20.85 | 0.13 | 1.64 | 0.02 | 1.60 | 0.03 | 1.54 | 0.02 | 7947 | 4.15 | 1.78 | 5.28 |
| 271 | 18.69 | 0.14 | 2.64 | 0.03 | 2.50 | 0.02 | 2.45 | 0.02 | 6673 | 4.30 | 1.33 | 5.89 |
| 272 | 20.9 | 0.39 | 4.21 | 0.04 | 3.86 | 0.05 | 3.75 | 0.04 | 5409 | 4.56 | 0.92 | 2.87 |
| 273 | 23.44 | 0.68 | 7.54 | 0.07 | 6.95 | 0.07 | 6.71 | 0.07 | 3454 | 4.93 | 0.35 | 4.69 |
| 274 | 23.11 | 0.68 | 6.11 | 0.07 | 5.54 | 0.07 | 5.27 | 0.07 | 3918 | 4.74 | 0.57 | 4.76 |
| 275 | 20.4 | 0.7 | 5.67 | 0.08 | 5.03 | 0.08 | 4.77 | 0.08 | 4202 | 4.68 | 0.65 | 5.39 |
| 276 | 22.58 | 0.66 | 5.27 | 0.07 | 4.69 | 0.07 | 4.55 | 0.07 | 4447 | 4.66 | 0.70 | 2.66 |
| 278 | 23.57 | 0.59 | 7.73 | 0.06 | 7.11 | 0.06 | 6.86 | 0.06 | 3425 | 4.96 | 0.32 | 4.67 |
| 279 | 21.8 | 0.68 | 6.11 | 0.07 | 5.48 | 0.07 | 5.25 | 0.07 | 3931 | 4.73 | 0.57 | 2.75 |
| 281 | 21.84 | 0.11 | 1.17 | 0.01 | 1.13 | 0.01 | 1.12 | 0.03 | 8185 | 4.02 | 1.98 | 5.04 |

Table A.1: continued.

| Hyades ID | parallax [mas] | parallax error [mas] | $M_J$ | $dM_J$ | $M_H$ | $dM_H$ | $M_K$ | $dM_K$ | $T_{eff}$ [K] | log($g$) (cgs) | Mass [M⊙] | Resolution [AU] |
|---|---|---|---|---|---|---|---|---|---|---|---|---|
| 283 | 36.13 | 0.68 | 8.09 | 0.05 | 7.54 | 0.04 | 7.26 | 0.04 | 3348 | 5.00 | 0.27 | 3.04 |
| 287 | 20.32 | 0.73 | 8.17 | 0.08 | 7.55 | 0.08 | 7.32 | 0.08 | 3339 | 5.01 | 0.26 | 2.46 |
| 288 | 22.26 | 0.53 | 4.89 | 0.05 | 4.37 | 0.06 | 4.26 | 0.05 | 4785 | 4.63 | 0.78 | 2.70 |
| 290 | 21.76 | 0.68 | 8.72 | 0.07 | 8.11 | 0.07 | 7.82 | 0.07 | 3241 | 5.06 | 0.20 | 2.30 |
| 291 | 19.49 | 0.21 | 2.51 | 0.03 | 2.38 | 0.03 | 2.34 | 0.03 | 6795 | 4.27 | 1.37 | 5.64 |
| 295 | 22.04 | 0.77 | 8.62 | 0.08 | 8.04 | 0.08 | 7.77 | 0.08 | 3254 | 5.05 | 0.20 | 2.27 |
| 297 | 19.45 | 0.22 | 4.01 | 0.04 | 3.65 | 0.05 | 3.48 | 0.04 | 5639 | 4.53 | 0.98 | 5.66 |
| 298 | 20.45 | 0.72 | 6.86 | 0.08 | 6.21 | 0.08 | 6.02 | 0.08 | 3629 | 4.84 | 0.46 | 5.38 |
| 301 | 19.02 | 0.35 | 4.88 | 0.05 | 4.38 | 0.05 | 4.23 | 0.04 | 4801 | 4.62 | 0.78 | 5.78 |
| 302 | 22.12 | 0.68 | 5.87 | 0.07 | 5.20 | 0.07 | 4.99 | 0.07 | 4071 | 4.70 | 0.61 | 4.97 |
| 304 | 28.67 | 0.68 | 6.20 | 0.06 | 5.60 | 0.07 | 5.35 | 0.06 | 3883 | 4.74 | 0.56 | 3.84 |
| 306 | 28.44 | 0.68 | 7.69 | 0.06 | 7.11 | 0.06 | 6.84 | 0.06 | 3428 | 4.95 | 0.33 | 3.87 |
| 307 | 21.37 | 0.59 | 6.91 | 0.06 | 6.27 | 0.06 | 6.05 | 0.06 | 3615 | 4.84 | 0.45 | 5.15 |
| 308 | 18.74 | 0.59 | 6.09 | 0.07 | 5.47 | 0.07 | 5.22 | 0.07 | 3940 | 4.73 | 0.58 | 5.87 |
| 309 | 21.27 | 0.05 | 0.73 | 0.28 | 0.70 | 0.23 | 0.72 | 0.47 | 8091 | 3.88 | 2.14 | 5.17 |
| 319 | 23.26 | 0.72 | 7.85 | 0.07 | 7.23 | 0.07 | 6.94 | 0.07 | 3406 | 4.97 | 0.31 | 2.15 |
| 325 | 22.02 | 0.06 | 0.31 | 0.03 | 0.30 | 0.02 | 0.22 | 0.02 | 8547 | 3.75 | 2.27 | 5.00 |
| 338 | 21.9 | 0.72 | 8.10 | 0.08 | 7.48 | 0.08 | 7.23 | 0.07 | 3354 | 5.00 | 0.27 | 2.28 |
| 340 | 21.09 | 0.22 | 3.00 | 0.03 | 2.79 | 0.03 | 2.76 | 0.03 | 6380 | 4.36 | 1.22 | 5.22 |
| 341 | 16.65 | 2.44 | 7.15 | 0.32 | 6.56 | 0.32 | 6.29 | 0.32 | 3544 | 4.88 | 0.41 | 3.00 |
| 344 | 22.56 | 0.22 | 3.19 | 0.03 | 2.99 | 0.04 | 2.92 | 0.03 | 6224 | 4.40 | 1.17 | 4.88 |
| 348 | 18.35 | 0.68 | 6.37 | 0.08 | 5.79 | 0.08 | 5.54 | 0.08 | 3800 | 4.77 | 0.53 | 5.99 |
| 349 | 20.22 | 0.09 | 1.69 | 0.02 | 1.63 | 0.02 | 1.58 | 0.02 | 7900 | 4.15 | 1.75 | 5.44 |

Table A.1: continued.

| Hyades ID | parallax [mas] | parallax error [mas] | M$_J$ | dM$_J$ | M$_H$ | dM$_H$ | M$_K$ | dM$_K$ | T$_{eff}$ [K] | log($g$) (cgs) | Mass [M$\odot$] | Resolution [AU] |
|---|---|---|---|---|---|---|---|---|---|---|---|---|
| 352 | 23.4 | 0.46 | 5.41 | 0.05 | 4.84 | 0.08 | 4.60 | 0.05 | 4367 | 4.66 | 0.69 | 4.70 |
| 353 | 20.22 | 0.77 | 8.20 | 0.09 | 7.58 | 0.09 | 7.32 | 0.08 | 3336 | 5.01 | 0.26 | 2.47 |
| 354 | 22.43 | 0.36 | 1.96 | 0.04 | 1.87 | 0.04 | 1.78 | 0.04 | 7586 | 4.19 | 1.63 | 0.00 |
| 359 | 22.37 | 0.12 | -0.23 | 0.02 | -0.31 | 0.02 | -0.33 | 0.03 | 7122 | 3.43 | 2.29 | 4.92 |
| 361 | 21.74 | 0.06 | 1.32 | 0.01 | 1.26 | 0.01 | 1.24 | 0.03 | 8160 | 4.06 | 1.92 | 5.06 |
| 367 | 21.46 | 0.58 | 6.34 | 0.06 | 5.70 | 0.06 | 5.49 | 0.06 | 3824 | 4.76 | 0.54 | 5.13 |
| 368 | 21.17 | 0.71 | 5.94 | 0.08 | 5.33 | 0.08 | 5.11 | 0.08 | 4009 | 4.71 | 0.60 | 2.83 |
| 370 | 21.86 | 0.16 | 2.73 | 0.03 | 2.47 | 0.04 | 2.42 | 0.03 | 6662 | 4.30 | 1.33 | 5.03 |
| 371 | 22.03 | 0.17 | 2.76 | 0.03 | 2.60 | 0.04 | 2.52 | 0.03 | 6578 | 4.31 | 1.30 | 4.99 |
| 373 | 20.78 | 0.3 | 4.81 | 0.04 | 4.28 | 0.04 | 4.10 | 0.04 | 4905 | 4.62 | 0.80 | 5.29 |
| 374 | 22.41 | 0.37 | 4.28 | 0.04 | 3.90 | 0.04 | 3.81 | 0.04 | 5346 | 4.57 | 0.91 | 2.68 |
| 378 | 23.15 | 0.68 | 6.35 | 0.07 | 5.72 | 0.07 | 5.48 | 0.07 | 3821 | 4.76 | 0.54 | 2.59 |
| 379 | 21.96 | 0.3 | 4.33 | 0.04 | 3.92 | 0.04 | 3.85 | 0.04 | 5305 | 4.57 | 0.90 | 5.01 |
| 386 | 21.81 | 0.06 | 1.15 | 0.01 | 1.10 | 0.01 | 1.08 | 0.03 | 8187 | 4.02 | 1.99 | 5.04 |
| 389 | 22.41 | 0.08 | 1.63 | 0.01 | 1.53 | 0.01 | 1.50 | 0.03 | 7974 | 4.14 | 1.79 | 4.91 |
| 397 | 21.63 | 0.17 | 2.81 | 0.04 | 2.62 | 0.03 | 2.57 | 0.03 | 6543 | 4.32 | 1.28 | 5.09 |
| 399 | 18.76 | 1.18 | 7.26 | 0.14 | 6.65 | 0.14 | 6.40 | 0.14 | 3518 | 4.89 | 0.40 | 5.86 |
| 400 | 21.13 | 0.81 | 8.83 | 0.09 | 8.23 | 0.09 | 7.93 | 0.09 | 3221 | 5.07 | 0.19 | 2.37 |
| 401 | 21.27 | 0.44 | 3.90 | 0.05 | 3.60 | 0.08 | 3.52 | 0.05 | 5677 | 4.52 | 0.99 | 5.17 |
| 403 | 21.94 | 0.77 | 8.00 | 0.08 | 7.41 | 0.08 | 7.11 | 0.08 | 3374 | 4.99 | 0.28 | 2.28 |
| 404 | 25.23 | 0.77 | 8.65 | 0.07 | 8.03 | 0.07 | 7.78 | 0.07 | 3252 | 5.05 | 0.20 | 1.98 |
| 405 | 19.34 | 0.21 | 3.17 | 0.03 | 3.00 | 0.06 | 2.89 | 0.03 | 6247 | 4.39 | 1.18 | 0.00 |
| 409 | 20.72 | 1.09 | 5.25 | 0.12 | 4.62 | 0.12 | 4.48 | 0.12 | 4499 | 4.65 | 0.71 | 2.90 |

Table A.1: continued.

| Hyades ID | parallax [mas] | parallax error [mas] | $M_J$ | $dM_J$ | $M_H$ | $dM_H$ | $M_K$ | $dM_K$ | $T_{eff}$ [K] | log($g$) (cgs) | Mass [M⊙] | Resolution [AU] |
|---|---|---|---|---|---|---|---|---|---|---|---|---|
| 410 | 24.01 | 0.15 | 2.49 | 0.03 | 2.29 | 0.02 | 2.23 | 0.03 | 6871 | 4.26 | 1.40 | 4.58 |
| 412 | 23.17 | 0.71 | 7.58 | 0.07 | 6.99 | 0.07 | 6.74 | 0.07 | 3447 | 4.94 | 0.34 | 4.75 |
| 415 | 17.01 | 0.75 | 7.92 | 0.10 | 7.35 | 0.10 | 7.04 | 0.10 | 3388 | 4.98 | 0.30 | 2.94 |
| 417 | 20.12 | 0.26 | 5.09 | 0.04 | 4.55 | 0.05 | 4.42 | 0.04 | 4603 | 4.64 | 0.74 | 2.98 |
| 419 | 22.11 | 0.76 | 7.57 | 0.08 | 6.95 | 0.08 | 6.71 | 0.08 | 3452 | 4.93 | 0.35 | 4.98 |
| 424 | 18.31 | 0.33 | 5.06 | 0.06 | 4.46 | 0.07 | 4.31 | 0.04 | 4682 | 4.63 | 0.75 | 6.01 |
| 428 | 23.27 | 0.4 | 5.26 | 0.04 | 4.67 | 0.04 | 4.52 | 0.05 | 4468 | 4.65 | 0.71 | 2.58 |
| 429 | 20.4 | 0.23 | 4.39 | 0.03 | 3.97 | 0.04 | 3.90 | 0.03 | 5247 | 4.58 | 0.88 | 2.94 |
| 431 | 24.39 | 0.71 | 7.84 | 0.07 | 7.26 | 0.07 | 6.98 | 0.07 | 3403 | 4.97 | 0.31 | 2.05 |
| 432 | 22.02 | 0.15 | 2.47 | 0.02 | 2.33 | 0.02 | 2.27 | 0.03 | 6849 | 4.26 | 1.39 | 5.00 |
| 433 | 22.27 | 0.21 | 0.91 | 0.02 | 0.83 | 0.02 | 0.81 | 0.04 | 8192 | 3.93 | 2.10 | 4.94 |
| 434 | 22.35 | 0.79 | 8.60 | 0.08 | 7.99 | 0.08 | 7.71 | 0.08 | 3261 | 5.05 | 0.21 | 2.24 |
| 439 | 18.6 | 0.29 | 4.41 | 0.04 | 4.02 | 0.04 | 3.90 | 0.04 | 5220 | 4.58 | 0.88 | 3.23 |
| 440 | 21.74 | 0.29 | 3.43 | 0.03 | 3.24 | 0.04 | 3.13 | 0.04 | 6035 | 4.44 | 1.10 | 5.06 |
| 455 | 19.82 | 0.25 | 4.35 | 0.03 | 3.99 | 0.03 | 3.86 | 0.03 | 5272 | 4.58 | 0.89 | 3.03 |
| 456 | 24.07 | 0.09 | 2.11 | 0.04 | 1.97 | 0.02 | 1.89 | 0.02 | 7423 | 4.21 | 1.58 | 4.57 |
| 459 | 23.02 | 0.72 | 6.59 | 0.07 | 5.96 | 0.07 | 5.75 | 0.07 | 3717 | 4.80 | 0.50 | 4.78 |
| 460 | 20.7 | 0.15 | 2.36 | 0.03 | 2.19 | 0.02 | 2.14 | 0.03 | 7027 | 4.24 | 1.45 | 5.31 |
| 461 | 52.1 | 0.23 | 4.53 | 0.02 | 3.98 | 0.02 | 3.82 | 0.02 | 5210 | 4.58 | 0.87 | 2.11 |
| 465 | 19.77 | 0.81 | 8.19 | 0.09 | 7.61 | 0.09 | 7.31 | 0.09 | 3335 | 5.01 | 0.26 | 2.53 |
| 466 | 19.88 | 0.81 | 8.13 | 0.09 | 7.56 | 0.09 | 7.28 | 0.09 | 3344 | 5.00 | 0.26 | 2.52 |
| 475 | 21.17 | 0.77 | 8.01 | 0.08 | 7.42 | 0.08 | 7.15 | 0.08 | 3370 | 4.99 | 0.28 | 2.36 |
| 478 | 23.47 | 0.15 | 3.31 | 0.03 | 3.05 | 0.02 | 3.01 | 0.03 | 6149 | 4.42 | 1.14 | 4.69 |

Table A.1: continued.

| Hyades ID | parallax [mas] | parallax error [mas] | $M_J$ | $dM_J$ | $M_H$ | $dM_H$ | $M_K$ | $dM_K$ | $T_{eff}$ [K] | log($g$) (cgs) | Mass [M$\odot$] | Resolution [AU] |
|---|---|---|---|---|---|---|---|---|---|---|---|---|
| 480 | 23.06 | 0.24 | 3.63 | 0.04 | 3.33 | 0.04 | 3.26 | 0.03 | 5914 | 4.47 | 1.06 | 4.77 |
| 486 | 23.12 | 0.51 | 4.91 | 0.05 | 4.42 | 0.05 | 4.30 | 0.05 | 4750 | 4.63 | 0.77 | 2.60 |
| 487 | 20.36 | 0.75 | 7.91 | 0.08 | 7.32 | 0.08 | 6.98 | 0.08 | 3395 | 4.98 | 0.30 | 2.46 |
| 489 | 23.2 | 0.3 | 5.57 | 0.04 | 4.89 | 0.03 | 4.74 | 0.04 | 4267 | 4.68 | 0.66 | 4.74 |
| 491 | 16.68 | 0.28 | 4.11 | 0.04 | 3.74 | 0.04 | 3.68 | 0.04 | 5511 | 4.55 | 0.95 | 3.60 |
| 496 | 14.05 | 1.13 | 8.57 | 0.18 | 7.94 | 0.18 | 7.66 | 0.18 | 3269 | 5.04 | 0.21 | 3.56 |
| 497 | 39.4 | 0.36 | 5.87 | 0.03 | 5.23 | 0.05 | 5.01 | 0.03 | 4070 | 4.70 | 0.61 | 2.79 |
| 498 | 15.48 | 0.16 | 3.55 | 0.03 | 3.25 | 0.03 | 3.18 | 0.03 | 5979 | 4.46 | 1.08 | 0.00 |
| 501 | 25.01 | 0.79 | 9.62 | 0.07 | 9.04 | 0.07 | 8.69 | 0.07 | 3059 | 5.16 | 0.13 | 2.00 |
| 502 | 14.51 | 0.19 | 3.92 | 0.04 | 3.59 | 0.05 | 3.50 | 0.03 | 5679 | 4.52 | 0.99 | 7.58 |
| 518 | 23.18 | 0.09 | 1.79 | 0.25 | 1.56 | 0.03 | 1.56 | 0.02 | 7971 | 4.14 | 1.79 | 4.75 |
| 525 | 15.71 | 0.14 | 0.98 | 0.03 | 1.00 | 0.04 | 0.95 | 0.03 | 8194 | 3.97 | 2.05 | 7.00 |
| 528 | 22.31 | 0.61 | 5.31 | 0.06 | 4.73 | 0.07 | 4.57 | 0.06 | 4424 | 4.66 | 0.70 | 2.69 |
| 539 | 22.29 | 0.72 | 6.02 | 0.07 | 5.38 | 0.07 | 5.15 | 0.07 | 3979 | 4.72 | 0.59 | 4.93 |
| 542 | 25.89 | 0.46 | 5.72 | 0.04 | 5.09 | 0.07 | 4.94 | 0.05 | 4144 | 4.69 | 0.63 | 4.25 |
| 544 | 19.04 | 0.46 | 5.09 | 0.07 | 4.53 | 0.06 | 4.39 | 0.06 | 4609 | 4.64 | 0.74 | 3.15 |
| 545 | 21.26 | 0.28 | 5.55 | 0.04 | 4.95 | 0.03 | 4.81 | 0.03 | 4239 | 4.68 | 0.66 | 2.82 |
| 549 | 27.6 | 0.27 | 5.63 | 0.03 | 5.08 | 0.03 | 4.92 | 0.03 | 4171 | 4.69 | 0.64 | 3.99 |
| 558 | 22.28 | 0.75 | 4.26 | 0.08 | 3.89 | 0.08 | 3.81 | 0.08 | 5354 | 4.57 | 0.91 | 4.94 |
| 566 | 20.89 | 0.18 | 3.24 | 0.03 | 3.03 | 0.03 | 2.95 | 0.02 | 6189 | 4.41 | 1.16 | 5.27 |
| 571 | 21.3 | 0.35 | 5.13 | 0.04 | 4.61 | 0.04 | 4.48 | 0.04 | 4547 | 4.65 | 0.73 | 5.16 |
| 576 | 20.3 | 0.16 | 2.86 | 0.03 | 2.68 | 0.03 | 2.60 | 0.02 | 6503 | 4.33 | 1.27 | 5.42 |
| 578 | 23.24 | 0.29 | 5.63 | 0.04 | 4.98 | 0.04 | 4.80 | 0.03 | 4219 | 4.68 | 0.65 | 4.73 |

Table A.1: continued.

| Hyades ID | parallax [mas] | parallax error [mas] | $M_J$ | $dM_J$ | $M_H$ | $dM_H$ | $M_K$ | $dM_K$ | $T_{eff}$ [K] | log($g$) (cgs) | Mass [M⊙] | Resolution [AU] |
|---|---|---|---|---|---|---|---|---|---|---|---|---|
| 581 | 19.61 | 0.15 | 1.43 | 0.26 | 1.03 | 0.04 | 0.95 | 0.02 | 8194 | 3.97 | 2.04 | 5.61 |
| 587 | 18.92 | 0.54 | 4.76 | 0.07 | 4.27 | 0.07 | 4.13 | 0.07 | 4920 | 4.61 | 0.81 | 5.81 |
| 596 | 16.06 | 0.11 | 1.76 | 0.03 | 1.69 | 0.02 | 1.65 | 0.02 | 7831 | 4.17 | 1.72 | 6.85 |
| 600 | 19.35 | 0.75 | 7.37 | 0.09 | 6.79 | 0.09 | 6.53 | 0.09 | 3490 | 4.91 | 0.38 | 5.68 |
| 604 | 17.99 | 0.2 | 5.04 | 0.04 | 4.54 | 0.03 | 4.39 | 0.03 | 4628 | 4.64 | 0.74 | 3.34 |
| 608 | 18.58 | 0.33 | 3.91 | 0.04 | 3.61 | 0.07 | 3.58 | 0.04 | 5648 | 4.53 | 0.98 | 5.92 |
| 618 | 23.08 | 0.1 | 2.67 | 0.03 | 2.51 | 0.03 | 2.46 | 0.02 | 6659 | 4.30 | 1.32 | 4.77 |
| 632 | 19.06 | 0.07 | 0.73 | 0.32 | 0.78 | 0.21 | 0.65 | 0.02 | 8056 | 3.86 | 2.15 | 5.77 |
| 635 | 18.54 | 0.37 | 3.97 | 0.05 | 3.64 | 0.05 | 3.57 | 0.05 | 5622 | 4.53 | 0.98 | 3.24 |
| 645 | 15.28 | 1.15 | 5.83 | 0.17 | 5.15 | 0.17 | 4.96 | 0.16 | 4098 | 4.70 | 0.62 | 7.20 |
| 663 | 20.77 | 0.76 | 7.47 | 0.08 | 6.84 | 0.08 | 6.62 | 0.08 | 3472 | 4.92 | 0.36 | 5.30 |
| 674 | 14.88 | 0.81 | 6.63 | 0.12 | 6.01 | 0.12 | 5.77 | 0.12 | 3703 | 4.80 | 0.49 | 7.39 |
| 676 | 17.41 | 0.4 | 3.90 | 0.05 | 3.60 | 0.08 | 3.51 | 0.05 | 5682 | 4.52 | 0.99 | 6.32 |
| 679 | 24.62 | 0.74 | 6.36 | 0.07 | 5.74 | 0.07 | 5.48 | 0.07 | 3815 | 4.76 | 0.54 | 4.47 |
| 686 | 16.02 | 1.25 | 5.80 | 0.17 | 5.15 | 0.17 | 4.94 | 0.17 | 4111 | 4.70 | 0.62 | 6.87 |
| 688 | 14.23 | 0.4 | 3.18 | 0.07 | 2.94 | 0.08 | 2.85 | 0.07 | 6256 | 4.39 | 1.18 | 7.73 |
| 697 | 19.43 | 0.12 | 1.50 | 0.02 | 1.44 | 0.03 | 1.38 | 0.03 | 8093 | 4.11 | 1.85 | 5.66 |
| 700 | 15.45 | 0.3 | 4.68 | 0.05 | 4.18 | 0.05 | 4.08 | 0.05 | 5000 | 4.61 | 0.82 | 7.12 |
| 706 | 15.53 | 1.85 | 5.87 | 0.26 | 5.25 | 0.26 | 5.09 | 0.26 | 4046 | 4.71 | 0.61 | 7.08 |
| 718 | 32.43 | 1.5 | 8.53 | 0.10 | 7.96 | 0.10 | 7.68 | 0.10 | 3269 | 5.04 | 0.21 | 3.39 |
| 719 | 23.46 | 1.57 | 7.14 | 0.15 | 6.52 | 0.15 | 6.27 | 0.15 | 3550 | 4.88 | 0.42 | 4.69 |
| 724 | 25.99 | 3.31 | 6.15 | 0.28 | 5.44 | 0.28 | 5.23 | 0.28 | 3936 | 4.73 | 0.58 | 4.23 |